https://doi.org/10.5194/egusphere-2026-3736
Preprint. Discussion started: 7 August 2026

Microstructural Heterogeneity Drives Tracer-Specific Systematic Bias in Darcy-Scale Flux Estimation

Ji-Young Baek[1], Byeong-Hak Park[2 †], Gabriel C. Rau[3 †], Kang-Kun Lee[4]

[1]Univ Rennes, CNRS, Géosciences Rennes, UMR 6118, 35000 Rennes, France
[2]Disposal Performance Demonstration R&D Division, Korea Atomic Energy Research Institute, Daejeon 34057, Republic of Korea.
[3] Earth Science Discipline - School of Science, The University of Newcastle, Callaghan NSW 2308, Australia
[4]School of Earth and Environmental Sciences, Seoul National University, Seoul 08826, Republic of Korea
† These authors contributed equally to this work.

Correspondence to: Kang-Kun Lee (kklee@snu.ac.kr)

Abstract. Complex microstructures are commonly simplified to a single continuum for interpreting Darcy-scale heat and solute transport, and tracers are often treated as interchangeable proxies for flux estimation. However, the specific impacts of microstructural heterogeneity on tracer-specific bias regimes remain poorly understood. We conducted controlled laboratory solute and heat tracer experiments using four sands with distinct grain size distributions, combined with micro-CT imaging and topological analysis of a controlled endmember pair. Although Darcy-scale analytical models reproduced observed breakthrough curves with excellent fidelity (mean $R^2 > 0.99$, NRMSE < 0.037), tracer-derived fluxes systematically underestimated independently measured Darcy fluxes in a tracer-specific manner. Solute fluxes were linearly underestimated by ~25% in the more heterogeneous sands, correlating with right-skewed pore-size distributions (skewness = 0.781) and non-Gaussian breakthrough behavior. In contrast, heat fluxes were nonlinearly and velocity-dependently underestimated, reaching up to 45% (including 19% spatial variability in volumetric heat capacity) in the most heterogeneous medium, with the solute-to-heat divergence ratio increasing with flow velocity. Micro-CT analysis revealed that the sand mixture possessed a more negative Euler number (−9,210 vs. −6,288) and exhibited representative elementary volume instability, indicating that tortuous pore connectivity amplifies local thermal non-equilibrium under fast flow. Conventional geostatistical metrics (e.g., Matérn smoothness) failed to distinguish these structural differences. These findings demonstrate that microstructural heterogeneity imposes physics-dependent, systematic biases that are invisible to standard continuum models and geostatistical descriptors, and that heat tracers become less reliable than solute tracers under high-velocity heterogeneous conditions. Process-aware metrics linking pore-network topology to transport behavior are needed to resolve these upscaling failures.

Keywords: Microstructural heterogeneity; Darcy flux; Heat tracer; Solute tracer; Upscaling problem

https://doi.org/10.5194/egusphere-2026-3736
Preprint. Discussion started: 7 August 2026

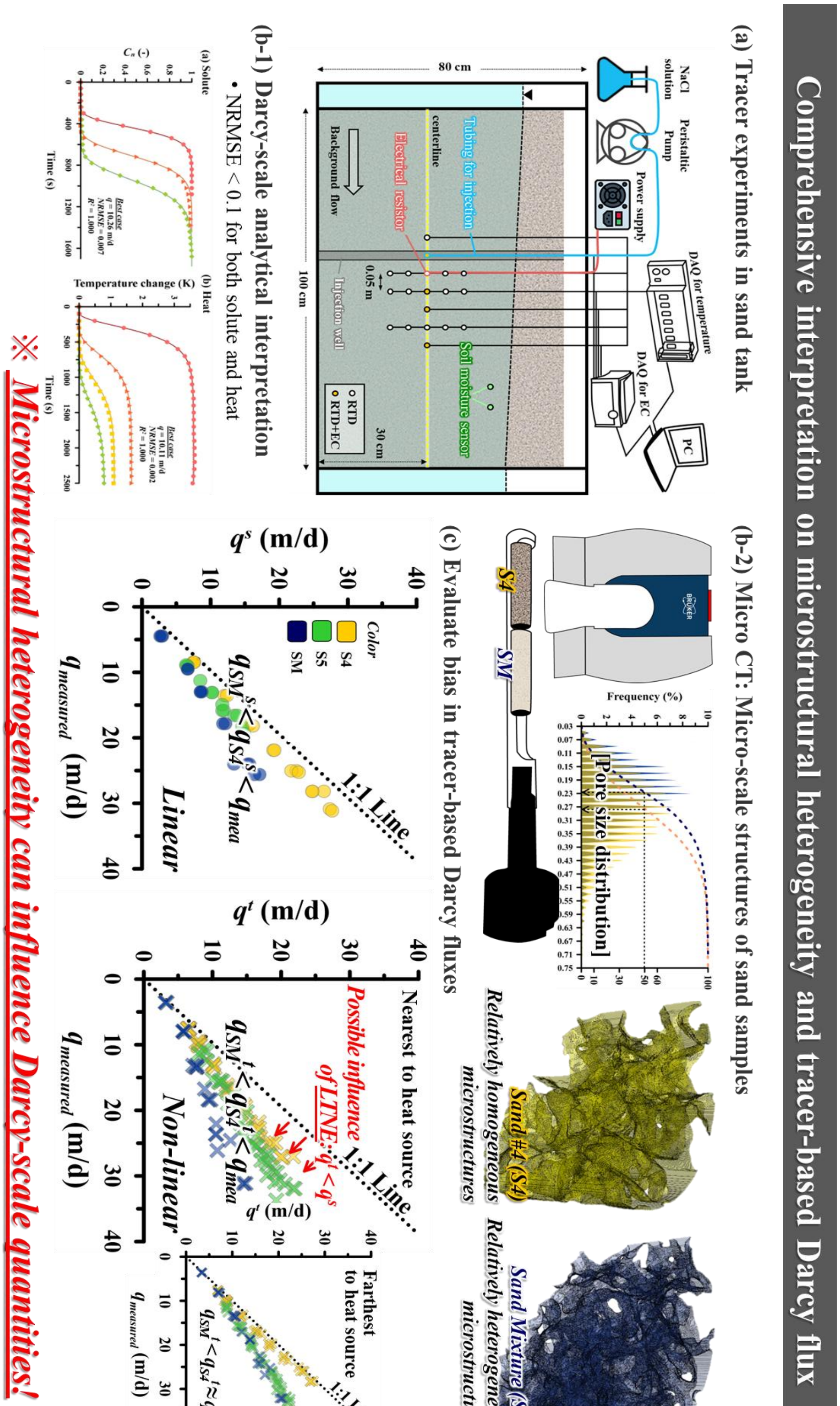

https://doi.org/10.5194/egusphere-2026-3736
Preprint. Discussion started: 7 August 2026

1 Introduction

Understanding transport processes in porous media is mandatory for economic and sustainable utilization of groundwater as hydraulic and thermal resources (Fetter, 2001; Freeze and Cherry, 1979; Stauffer et al., 2013). In practice, groundwater flow and transport within an aquifer has been described with the volume-averaged parameters of a well-selected control volume that is large enough to represent the target aquifer (Bear, 1972). Through volume-averaging, the complicated characteristics in small-scale areas were inevitably simplified by aggregating into volume-averaged parameters. For example, when modelling alluvial aquifers in the field, it generally assumes layered heterogeneity based on hydrofacies (Davis et al., 1997) in assigning single hydraulic conductivity which ignores small-scale heterogeneity within each layer. For heat transport in porous media, an additional simplification is frequently invoked: local thermal equilibrium (LTE), where the solid and neighboring fluid are assumed to reach instantaneous thermal equilibrium so that they share the same temperature in a representative elementary volume. LTE is typically assumed in many hydrogeological applications based on the sufficiently low groundwater flow velocity that guarantees enough time for thermal equilibrium (Rau et al., 2012a). Under these simplifications, both conservative solute and heat tracers have been widely treated as interchangeable proxies for estimating Darcy flux, with their front velocities converted to bulk flow via porosity or heat-capacity ratios (Anderson, 2005; Irvine et al., 2015; Sudicky, 1986).

Yet, small-scale phenomena that are typically ignored in these simplifications can substantially influence the larger-scale transport interpretation (Irvine et al., 2015; Irvine et al., 2016; Yin et al., 2023). Yin et al. (2023) pointed out that the small-scale heterogeneity within sub-hydrofacies significantly contributed to better prediction of transport in layered heterogeneous aquifers. Likewise, violation of LTE (referred to as local thermal non-equilibrium, LTNE) may become influential in shallow aquifers and its occurrence can be amplified by hydraulic conductivity contrasts (Hamidi et al., 2019; Shi et al., 2025) and small-scale nonuniform flow (Baek et al., 2022; Lee et al., 2025). These examples collectively suggest that microstructural heterogeneity and the resulting nonuniform flow can propagate across scales, altering the accurate prediction of heat transport at the Darcy scale. However, the specific impacts of microstructural heterogeneity on Darcy-scale transport parameter estimation have been poorly understood from a practical point of view, particularly with respect to how identical pore structures may generate fundamentally different, tracer-specific bias regimes. While complex pore networks and local variations in particle size distribution can create preferential pathways or impede flow, thereby affecting overall transport dynamics (Afshari et al., 2020), the differential consequences for solute versus heat tracers remain unresolved.

Recently, motivated by growing demand for upscaling for practical applications (Zhang et al., 2021), a few studies have overcome the challenge of scale disparity due to extremely high computational cost to make reliable predictions on representative volumes (Mehmani and Tchelepi, 2018) and have increasingly highlighted the critical impact of microstructural heterogeneity when applying Darcy-scale approaches, demonstrating that microscale interactions can significantly alter bulk transport parameters (Afshari et al., 2020; Ilgen et al., 2024; Qu et al., 2024). This understanding underscores the need to bridge the gap between pore-scale observations and Darcy-scale models to achieve accurate predictions. Despite the growing

https://doi.org/10.5194/egusphere-2026-3736
Preprint. Discussion started: 7 August 2026

recognition of the need to bridge microstructural heterogeneity and Darcy-scale transport, practical approaches based on systematic experimental studies on the specific impacts of microstructural heterogeneity on Darcy-scale transport parameter estimations remain limited.

To address this knowledge gap, the present study examines the effects of microstructural heterogeneity on transport parameter estimation within Darcy-scale analytical frameworks, using controlled laboratory experiments supported by micro-CT imaging and geostatistical analysis. We hypothesize that microstructural heterogeneity generates tracer-specific bias regimes: solute fluxes will be linearly underestimated via non-Gaussian mechanical dispersion, whereas heat fluxes will be nonlinearly underestimated via local thermal non-equilibrium, with the divergence increasing in more heterogeneous media. The transport behaviors of solute and heat in the porous media of three relatively homogeneous single-numbered sands and a mixture of three sands were analyzed using Darcy-scale analytical models. By characterizing the distinct transport behavior of the sand mixture, the influence of microstructural heterogeneity on Darcy-scale quantities was interpreted. In addition, micro-CT imaging was applied to support the existence of distinct microstructural heterogeneity of sands. Based on these CT images, geostatistical and topological measures were derived for the sands to assess their potential applicability in quantifying microstructural heterogeneity and enabling the bridging of pore-to Darcy-scale interpretations.

2 Material and methods

2.1 Comparative study on solute and heat tracer experiments using different types of sand

To examine the influence of microstructural heterogeneity on the Darcy-scale (here, cm-scale) interpretation of solute and heat transport within natural porous media, we conducted a series of laboratory experiments involving four distinct sand types: three relatively homogeneous sands (referred to as single-numbered sands—Sand #3, Sand #4, and Sand #5—in previous studies) and a mixture of these sands (Sand Mixture). Figure 1a shows the laboratory experimental setup which consists of an acrylic tank with dimensions of 1.3 m × 0.6 m × 0.8 m (L × W × H). The tank was composed of a central sand tank and two side water chambers. Within the central sand tank, microelectrodes (Microelectrodes, USA) and thermometers (Pt100, Hayashi Denko, Japan) were strategically positioned to facilitate measurement of fluid electrical conductivity (EC) and temperature during tracer experiments. All data was digitized and recorded through a data acquisition (DAQ) system which consists of isoPods (EP357, eDAQ, Australia) and resistance temperature detector input modules (NI-9217, National Instruments, USA) coupled to a CompactDAQ chassis (cDAQ-9178, National Instruments, USA). Prior to each transport experiment, we undertook an initialization phase to eliminate any residual tracers from the porous medium, ensuring pristine initial conditions.

https://doi.org/10.5194/egusphere-2026-3736
Preprint. Discussion started: 7 August 2026

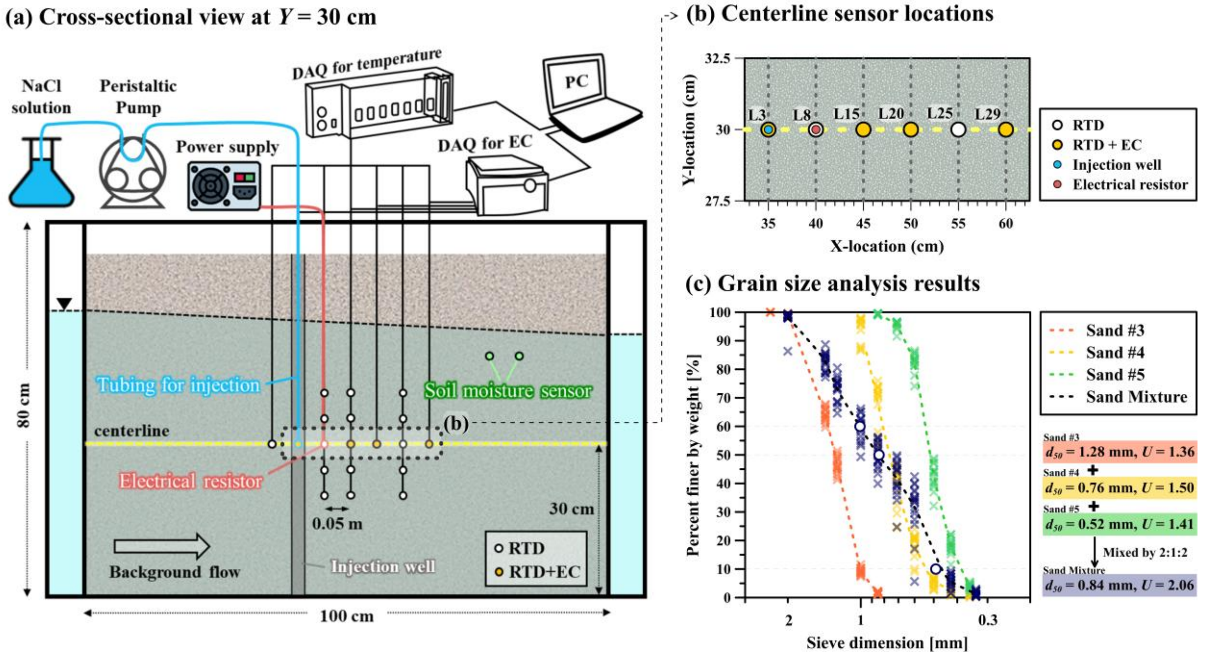

Figure 1: Overview of the laboratory experimental setup: (a) Schematic diagram of the sand tank, measurement, and data acquisition system (after Baek et al., 2022); (b) sensor locations aligned in the centerline (Baek et al., 2024); (c) grain size analysis results for the natural sands used (after Park, 2019 and Baek et al., 2024).

This experimental setup was designed and used in previous studies to investigate the relationship between flow velocity and dispersion (Baek et al., 2024), assess the impact of the thermal dispersivity and its ratio during heat transport (Park et al., 2018; Park and Lee 2021), and explore the presence of local thermal non-equilibrium heat transport (Baek et al., 2022). Building upon previous experiments conducted with three sand types, we additionally performed a new experiment using a relatively heterogeneous sand. All experiments employed the same laboratory system but used four different types of sand to examine how pore-scale heterogeneity influences the estimation of Darcy-scale transport parameters for heat and solute transport.

All solute tracer experiments were conducted following the same tracer injection protocols as outlined in Baek et al. (2022). A conservative tracer, 500 ppm sodium chloride (NaCl) solution (99.5%, Junsei Chemical, Japan), was injected into location L3 (Fig. 1b) for a duration of 1 minute at a flow rate of 50 ml/min. The concentration of the solution was carefully determined to avoid any additional density effects that might interfere with the estimation of transport parameters (e.g., see Schinacariol and Schwartz, 1990). Four microelectrodes were positioned at locations L3, L15, L20, and L29 (as indicated in Fig. 1b) to monitor changes in EC along the direction of flow. Sensors were linked to the DAQ system and the signal was monitored on a computer via PodVu software (eDAQ, Australia) to record the fluid's EC values at 1-second intervals (i.e., 1 Hz) during each experiment.

https://doi.org/10.5194/egusphere-2026-3736
Preprint. Discussion started: 7 August 2026

For heat tracer experiments, we followed the same procedure as described in Park (2019). As a point heat source, we employed an electrical resistor with a 7 mm diameter, a resistance of 47 Ω, and a power output rating of 5 W which was positioned at location L8 in Fig. 1b. To apply a constant power ranging from 2.266 to 4.495 W we used a laboratory DC power supply with an AC input of 220 V and an adjustable DC output of 0–30 V. Following each heat experiment, a continuous water flow was maintained to achieve thermal equilibrium with the inlet, while temperature changes were monitored using 29 sensors connected to a DAQ system. DAQ software (DAQmx and LabVIEW 2015) enabled the real-time monitoring of temperature signals on the computer. Temperature readings were recorded at 0.1-second intervals (i.e., 10 Hz) throughout each experiment.

As natural porous materials, four different grain size distributions of silica sand (dry sand, Joomoonjin Silica Sand Co., Ltd., Republic of Korea) were used: Sand #3 (S3; 8–16 mesh), Sand #4 (S4; 20–30 mesh), Sand #5 (S5; 30–60 mesh), and finally Sand Mixture (SM). To broaden the grain size distribution, three sands (S3, S4, and S5) were mixed in a 2:1:2 ratio using a concrete mixer (DKM-230C; DaeKwang Construction Machinery Co., Ltd., Republic of Korea), ensuring thorough randomization of particles to create the Sand Mixture. Since the sand tank volume was much larger than the concrete mixer (maximum 230 L), the mixing process was conducted repeatedly 16 times. For every mixing cycle, the mixture of sand was sampled for grain size analysis. The grain size analysis results, as visually depicted in Fig. 1c, showed that the grain size distribution of SM ranged from the minimum grain size of S5 (the finest dry sand) to the maximum grain size of S3 (the coarsest dry sand) with a similar mean grain size (d_{50}) of 0.84 mm to S4 (d_{50} = 0.76 mm). Uniformity (U) of SM was increased to 2.06 compared to that of other sands (1.36–1.50). The weight percentage that passed the sieves also showed a greater variability across analyses compared to other sands (see Table 1). The values of mean grain size indicate the presence of very coarse to coarse sand as defined by Friedman and Sanders (1978).

Physical and hydraulic parameters for S3, S4, and S5 were carefully estimated in Park (2019). He analyzed the mineral proportion of sand samples using X-ray diffraction (XRD) analysis indicating that high portion of quartz for all sands (68–76%). The pore volume was measured in a laboratory using a burette and graduated cylinder for at least 16 samples and the mean porosity was determined to be 0.367 ± 0.005 for S3, 0.374 ± 0.005 for S4, 0.377 ± 0.006 for S5, and 0.324 ± 0.007 for SM. Hydraulic conductivity was evaluated by a constant-head permeameter as ranging between 7 and 14 cm/min for all sands. The physical and thermal characteristics of all used sands are outlined in Table 1.

https://doi.org/10.5194/egusphere-2026-3736
Preprint. Discussion started: 7 August 2026

Table 1 Hydraulic, physical and thermal properties of used porous media.

Porous medium	Property	Value	Classification	Comment	Reference
Sand #3 (S3)	d_{50}^{1} [mm]	1.28 ± 0.005	Very coarse sand*	Sieve analysis	[1]
	U^{2} [-]	1.36 ± 0.01	-	Sieve analysis	[1]
	K^{3} [cm/min]	14.0 ± 0.4	Sand or gravel**	Constant-head permeameter	[1]
	n^{4} [-]	0.367 ± 0.005	Sand or gravel or silt**	Experiments	[1]
	ρc [MJ/m^3/K]	2.78 ± 0.0592	Sand or silt***	Heat tracer test under no flow	[1]
	λ [W/m/K]	1.954 ± 0.107	Sand or gravel or silt***	Heat tracer test under no flow	[1]
Sand #4 (S4)	d_{50}^{1} [mm]	0.76 ± 0.010	Coarse sand*	Sieve analysis	[1]
	U^{2} [-]	1.50 ± 0.03	-	Sieve analysis	[1]
	K^{3} [cm/min]	10.2 ± 0.3	Sand or gravel**	Constant-head permeameter	[1]
	n^{4} [-]	0.374 ± 0.005	Sand or gravel or silt**	Experiments	[2]
	ρc [MJ/m^3/K]	2.80 ± 0.0349	Sand or silt***	Heat tracer test under no flow	[2]
	λ [W/m/K]	1.908 ± 0.078	Sand or gravel or silt***	Heat tracer test under no flow	[2]
Sand #5 (S5)	d_{50}^{1} [mm]	0.52 ± 0.003	Coarse sand*	Sieve analysis	[1]
	U^{2} [-]	1.41 ± 0.01	-	Sieve analysis	[1]
	K^{3} [cm/min]	7.8 ± 0.1	Sand or gravel**	Constant-head permeameter	[1]
	n^{4} [-]	0.377 ± 0.006	Sand or gravel or silt**	Experiments	[3]
	ρc [MJ/m^3/K]	2.68 ± 0.124	Sand or silt***	Heat tracer test under no flow	[3]
	λ [W/m/K]	2.001 ± 0.165	Sand or silt***	Heat tracer test under no flow	[3]
Sand Mixture (SM)	d_{50}^{1} [mm]	0.84 ± 0.09	Coarse sand*	Grain size analysis	[4]
	U^{2} [-]	2.06 ± 0.19	-	Sieve analysis	[4]
	K^{3} [cm/min]	9.3 ± 0.2	Sand or gravel**	Constant-head permeameter	[4]
	n^{4} [-]	0.324 ± 0.007	Sand or gravel or silt**	Experiments	[4]
	ρc [MJ/m^3/K]	2.71 ± 0.147	Sand or silt***	Heat tracer test under no flow	[4]
	λ [W/m/K]	1.960 ± 0.120	Sand or gravel or silt***	Heat tracer test under no flow	[4]

$^{1}d_{50}$: mean grain size, ^{2}U: uniformity, ^{3}K: hydraulic conductivity, ^{4}n: porosity
* Friedman and Sanders, 1978 ** Freeze and Cherry, 1979 *** values for saturated sediments. Stauffer et al., 2013
[1] Park, 2019 [2] Baek et al., 2022 [3] Baek et al., 2024 [4] Current study

To enable a comparative analysis of transport processes in water-saturated porous media of varying particle size distributions, this study adopted solute and thermal transport parameter values from earlier studies: those for S3 provided in Park (2019), and for S4 and S5 found in Baek et al. (2024). For the SM, solute transport experiments were conducted at 15 distinct Darcy fluxes ranging from 4.66 to 31.22 m/d. Heat tracer experiments were conducted for (i) no-flow conditions to derive thermal parameters, and for (ii) a range of flow conditions with flux rates varying from 4.89 to 30.23 m/d. All tracer experiments were conducted independently using the same experimental apparatus. Darcy fluxes were carefully calculated from the measured volumetric flow rate of the outlet tank and the cross-sectional area of flow, ensuring direct and reliable comparison between the two tracers. A detailed summary of the testing conditions for the four sand types is provided in Table 2.

https://doi.org/10.5194/egusphere-2026-3736
Preprint. Discussion started: 7 August 2026

Table 2. Summary of experimental conditions (after Baek et al. (2024), and Park (2019)).

Porous material	Experiment	No flow (Heat)	Horizontal flow (Solute)	Horizontal flow (Heat)	Reference
Sand #3 (S3)	Runs	1	-	10	Park, 2019
	Darcy velocity range	-	-	–40.38 m/d	
	Tracer input	Step input 4.71 W	-	Step input 4.71 W	
Sand #4 (S4)	Runs	7	18	34	Baek et al., 2022
	Darcy velocity range	-	8.9–36.5 m/d	8.1–36.8 m/d	
	Tracer input	Step input 2.27–4.52 W	Finite pulse input For 1 minute by 50 ml/min	Step input 2.94–4.52 W	
Sand #5 (S5)	Runs	10	15	41	Baek et al., 2024
	Darcy velocity range	-	10.4-30.1 m/d	12.3–39.3 m/d	
	Tracer input	Step input 2.27–4.50 W	Finite pulse input For 1 minute by 50 ml/min	Step input 2.27–4.50 W	
Sand Mixture (SM)	Runs	6	15	25	Current study
	Darcy velocity range	-	4.7-36.2 m/d	4.9–30.3 m/d	
	Tracer input	Step input 3.07–3.80 W	Finite pulse input For 1 minute by 50 ml/min	Step input 3.17–4.24 W	

2.2 Darcy-scale analytical modeling of solute and heat transport

In the current study, to unveil the influence of pore structure complexity on continuum-scale transport interpretation, analytical models established for Darcy-scale were applied to obtain transport parameters (i.e., tracer front velocity, and dispersion coefficient) of different sized sands. At the continuum scale, if instantaneous thermal equilibrium between the solid and adjacent fluid can be assumed, the advective–dispersive transport of both solute and heat within a representative elementary volume (REV) is described by a differential transport equation (DTE) (de Marsily, 1986) as follows:

$$\frac{\partial S}{\partial t} = D\nabla^2 S - v\nabla S \tag{1}$$

where S is the concentration [kg/m^3] or temperature [K], D is the tracer dispersion coefficient [m^2/s], and v is the tracer front velocity [m/s]. Under no-flow conditions, advective transport can be ignored, and thus Eq. (1) can be rewritten as

https://doi.org/10.5194/egusphere-2026-3736
Preprint. Discussion started: 7 August 2026

$$\frac{\partial S}{\partial t} = D\nabla^2 S. \tag{2}$$

Hunt (1978) solved the DTE (Eq. (1)) for solute transport under groundwater flow, assuming a continuous point source moving along the x direction with a source strength M [kg/s] to address pollution problems occurred in hydrogeological environments.
160 The resulting solution is given by the following equation:

$$C(x,y,z,t) = \frac{M}{8\pi n_e r D_T^s} exp\left(\frac{xv^s}{2D_L^s}\right)\left[exp\left(-\frac{rv^s}{2D_L^s}\right) erfc\left(\frac{r-v^s t}{2\sqrt{D_L^s t}}\right) + exp\left(-\frac{rv^s}{2D_L^s}\right) erfc\left(\frac{r+v^s t}{2\sqrt{D_L^s t}}\right)\right] \tag{3}$$

with the initial condition of

$$C(x,y,z,t\ =\ 0) = C_0 = 0\ for\ -\infty < (x,y,z) <\ \infty \tag{4}$$

and the radial distance given by

165 $$r = \sqrt{x^2 + \frac{D_L^s}{D_T^s}(y^2 + z^2)} \tag{5}$$

where n_e is the effective porosity [-], and the superscript s indicates that the parameter pertains to solute transport. In the case of solute transport, as detailed in Rau et al. (2012a), and Baek et al. (2022), Eq. (3) was normalized to disregard the potential influences of hydraulic pressure on EC monitoring by dividing $C(x, y, z, t \to \infty)$ as

$$C_n(r,t) = \frac{1}{2}\left[erfc\left(\frac{r-v^s t}{2\sqrt{D_L^s t}}\right) + exp\left(\frac{rv^s}{D_L^s}\right) erfc\left(\frac{r+v^s t}{2\sqrt{D_L^s t}}\right)\right] \tag{6}$$

170 where C_n is the normalized concentration [–] ranging between 0 and 1. Here, we call this analytical model as normalized moving continuous point source (NMCPS) model.

For heat transport under local thermal equilibrium within porous media, assuming that a point source located at the origin of an infinite porous medium that continuously operates ($W(0,0,0,t > 0) = Q$) under the uniform flow in the x direction, Eq. (1) for heat transport was originally solved by Carlslaw and Jaeger (1959), and later modified by Rau et al. (2012a) with the
175 initial condition of $T(x,y,z,t = 0\ ) = T_0$ and boundary condition of $\lim_{x,y,z\to\infty} T(x,y,z,t) = T_0$ as

$$T(x,y,z,t) = T_0 + \frac{Q}{8\pi D_T^t \rho c r'} exp\left(\frac{xv^t}{2D_L^t}\right)\left[exp\left(-\frac{r'v^t}{2D_L^t}\right) erfc\left(\frac{r'-v^t t}{2\sqrt{D_L^t t}}\right) + exp\left(\frac{r'v^t}{2D_L^t}\right) erfc\left(\frac{r'+v^t t}{2\sqrt{D_L^t t}}\right)\right] \tag{7}$$

with the radial distance defined as below:

$$r' = \sqrt{x^2 + \frac{D_L^t}{D_T^t}(y^2 + z^2)} \tag{8}$$

https://doi.org/10.5194/egusphere-2026-3736
Preprint. Discussion started: 7 August 2026

where Q is the source strength [W], ρc is the volumetric heat capacity of control volume [MJ/m^3/K], subscript L denotes the longitudinal direction, T denotes the transverse direction, and superscript t indicates parameter related to heat transport. With same initial and boundary conditions, when only considering conduction within the porous medium, Eq. (2) for heat transport can be solved as (Carslaw and Jaeger, 1959)

$$T(x,y,z,t) = T_0 + \frac{Q}{8\pi D_0^t \rho c r'} erfc\left(\frac{r'}{\sqrt{4D_0^t t}}\right) \tag{9}$$

where D_0^t is the thermal diffusion coefficient [m^2/s], which indicates how fast the thermal energy can be diffused into the porous medium. Equations (7) and (9) are also known as the moving continuous point source (MCPS) and continuous point source (CPS) models, respectively.

For the analytical modeling of the conducted tracer experiments, the fitting between the analytical solutions and obtained time-series data was progressed by minimizing the squares of residual sum using nonlinear least squares methods implemented in MATLAB. The quality of fitting results was quantified by normalized root mean square error (NRMSE) defined as

$$NRMSE = \sqrt{\frac{\sum_{i=1}^{N}(S_i - O_i)^2}{\sum_{i=1}^{N}(O_i)^2}} \tag{10}$$

where S_i is the ith predicted data, and O_i is the ith observed data. In case of solute tracer experiments, the observed EC time series were integrated over time and normalized for finite pulse input to match the form of the NMCPS model (Eq. (6)). During the data preprocessing, the diffusion coefficient of sodium chloride in free water (1.47×10^{-9} m^2/s), reported by Vitagliano and Lyons (1956), was utilized. As a result, the solute front velocities (v_{fit}^s) and solute dispersion coefficients (D_{fit}^s) were estimated for each experiment. Similarly, the thermal front velocities (v_{fit}^t) and thermal dispersion coefficients (D_{fit}^t) were estimated for heat transport experiments conducted at various flow velocities by the MCPS model (i.e. Eq. (7)). Unlike solute, however, since thermal diffusivity depends on the properties of used porous medium, the thermal properties of sand were estimated by fitting the temperature time-series data obtained from heat transport experiments under no-flow condition to the CPS model in Eq. (9).

For further analysis to assess the influence of pore-scale heterogeneity on groundwater flow velocity estimates, an additional comparison was conducted between measured Darcy flux ($q_{measured}$, [m/s])—based on in-situ flow rate measurements—and solute- or heat-based Darcy fluxes (q^s, q^t [m/s])—calculated using tracer front velocities (v_{fit}^s, v_{fit}^t) obtained from analytical modeling. Each tracer front velocity can be expressed with Darcy flux (q, [m/s]) as (Rau et al., 2012a)

$$v^s = \frac{q}{n_e} \tag{11}$$

$$v^t = \frac{\rho_w c_w}{\rho c} q \tag{12}$$

https://doi.org/10.5194/egusphere-2026-3736
Preprint. Discussion started: 7 August 2026

where the subscript w denotes the water. Stemmed from Eqs. (11) and (12), the effective Darcy fluxes of solute and heat base d on tracer front velocities (Eqs. 6 and 7) can be rearranged as

$$q^s = n_e v_{fit}^s \tag{13}$$

$$q^t = \frac{\rho c}{\rho_w c_w} v_{fit}^t \tag{14}$$

Here, the ratio between q^s and q^t can be expressed using apparent and effective retardation factor (R_{app}, and R_{eff}) suggested b y Gossler et al. (2019) as

$$q^s/q^t = \frac{n_e v_{fit}^s}{\frac{\rho c}{\rho_w c_w} v_{fit}^t} = \frac{v_{fit}^s}{v_{fit}^t}\left(1/\frac{\rho c}{n_e \rho_w c_w}\right) = R_{eff}/R_{app} \tag{15}$$

where

$$R_{eff} = \frac{v_{fit}^s}{v_{fit}^t} \tag{16}$$

$$R_{app} = \frac{\rho c}{n_e \rho_w c_w} \tag{17}$$

Since the experimental system represents an unconfined aquifer, the hydraulic head is a function of distance along the flow d irection. The steady-state flow in the x direction within experimental system can be described by Darcy's law as

$$Q = qA = q(x)\, w\, h(x) \tag{18}$$

where Q is the volumetric flow rate measured at the outlet tank [m^3/s], $q(x)$ is the local Darcy flux at x [m/s], w is the aquife r width [m] (here, the width of sand tank), and $h(x)$ is the hydraulic head at x [m]. Thus, the measured Darcy flux ($q_{measured}$) is also the function of x. Assuming the Dupuit approximation without consideration of infiltration and evapotranspiration, Eq. (18) can be expressed as

$$q_{measured}(x) = \frac{Q}{wh(x)} = \frac{Q}{w\sqrt{h_1^2 - \frac{(h_1^2 - h_2^2)x}{L}}} \tag{19}$$

where h_1 and h_2 are the hydraulic heads at the inlet and outlet tank [m], and L is the length of the sand tank [m]. For uncertainty assessment of Darcy flux estimates from solute and heat tracers (q^s, and q^t), these flux estimates—calculated via Eqs. (13) and (14)—are directly compared with $q_{measured}$ corrected by Eq. (19). Because the unconfined flow field yields a spatially varying Darcy flux, q(x) was corrected via Eq. (18) at the x-coordinate of each monitoring location (L3: x ≈ 35 cm; L8: x ≈ 40 cm; L15: x ≈ 45 cm; L20: x ≈ 50 cm; L25: x ≈ 55 cm; L29: x ≈ 59 cm; see Fig. 1b). To compare the tracer-derived and measured Darcy flux, this study defined the ratio between them as

$$\Gamma^{s,t} = q^{s,t}/q_{measured} \tag{20}$$

where superscript s indicates solute- and t indicates thermal-derived.

https://doi.org/10.5194/egusphere-2026-3736
Preprint. Discussion started: 7 August 2026

2.3 Micro-CT imaging and image processing

S4 and SM were selected for microstructural heterogeneity because their similar mean grain sizes ($d_{50} \approx 0.76$ vs. 0.84 mm) but contrasting uniformity coefficients (U = 1.50 vs. 2.06) create a controlled natural experiment that isolates pore-network complexity from grain-size effects. The actual pore structures of sand samples were represented using images obtained by an X-ray micro-CT scanner (SkyScan 1276, Bruker Corporation, Germany) at the Common Research Facility of Biological Sciences, Seoul National University. For micro-CT image analysis, sand samples were wet packed with water within a customized acrylic mold (11 mm inner diameter, 61.5 mm height). The sand was packed up to a height of 40 mm, yielding a bulk volume of 3.8 ml. Each sample was placed on a 16 mm bedding before being mounted onto the scanner. Scanning process was performed using an X-ray source set to 70 kV and 57 μA. The scanning resolution was optimized to 10 μm by adjusting the source intensity and detector resolution. Since scanning conditions are not standardized, they were optimized according to the specific characteristics of each sample. To minimize diffuse reflection effects, the X-ray source underwent a full 360° spiral rotation during scanning. A summary of the scanning parameters is presented in Table 3.
The scanned images were reconstructed using the NRecon® software (Bruker Corporation, Germany) while compensating for misalignment and correcting artifacts such as beam hardening, and ring artefacts. A region of interest (ROI) was selected as a circular area with a diameter of 9.35 mm, thereby eliminating potential wall effects from the packing process. Following image reconstruction, the segmentation process to distinguish pore space and grain was performed using CT Analyser (CTAn, Bruker Corporation, Germany).
After segmentation, the resulting CT images were binarized using value 0 for pore and 1 for grain. By stacking each image in high-resolution, a three-dimensional indicator field was constructed to represent the pore structure of the target medium (Adler and Thovert, 1998). CTAn provided the size distributions of pore and grain and normality of that distribution was evaluated by calculating the statistical measure: skewness and kurtosis. Also, the heterogeneity of pore size was additionally assessed by coefficient of variance defined as the ratio of mean and standard deviation. Using this indicator field, which consists of 0 and 1, porosity can be directly calculated as the ratio of pore voxels to total voxels. By varying the size of the sampling volume, the porosity within the control volume for each medium was explored. From the volumetric analysis, the representative elementary volume of each sand was identified as the minimum control volume size beyond which the coefficient of variation of porosity, calculated from 1,000 randomly sampled volumes, remained consistently below 10%. Sizes of grains and pores were characterized from the high-resolution micro CT images using CT Analyser software. Examples of the resulting CT images of the two sand types (S4 and SM) are shown in Fig. 2.

https://doi.org/10.5194/egusphere-2026-3736
Preprint. Discussion started: 7 August 2026

Table 3. Scanning and reconstruction conditions in the present study.

Conditions		Unit	Value
Scanning	Power of voltage	kV	70
Scanning	Current	μA	57
Scanning	Voxel dimension (x, y, z)	μm	10.00×10.00×10.00
Scanning	Number of voxels (x, y, z)	-	1968×2688×1532
Reconstruction	Number of pixels in ROI	pixels	936
Reconstruction	Number of views	pixels	2106

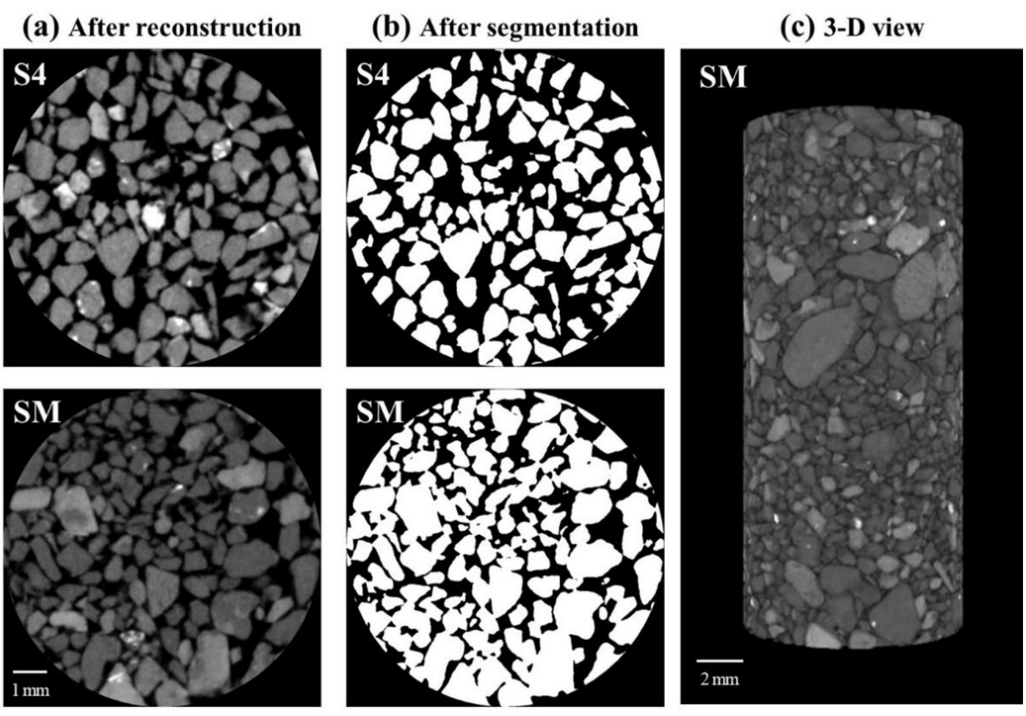

Figure 2: Examples of micro CT images for sand S4 and SM after reconstruction (a), after segmentation (b), and in 3-D view (c)

https://doi.org/10.5194/egusphere-2026-3736
Preprint. Discussion started: 7 August 2026

2.4 Quantification of pore-network complexity

To feasibly incorporate this understanding into Darcy-scale transport modeling, a quantitative parameter that enables the linkage between pore structure and Darcy-scale behavior is needed. In this context, this study adopted two measures which can represent microstructural complexity. First, Euler number is one of measures that represents connectedness of pore structures (Vogel and Ruth, 2001; Pires et al., 2020). Next, a geostatistical metric called smoothness parameter as the measure of pore roughness which was adopted by Di Palma et al. (2017). The resulted quantitative microstructure heterogeneities were compared to the results of normality deviation that can be represented by skewness and kurtosis for the linkage to Darcy-scale behavior. Skewness and kurtosis were obtained by computing third and fourth temporal moments of each time-series data at all monitoring locations for both solute and heat. The resulted 3-D CT data was used to derive geostatistical properties related to the pore network: Euler number, and pore roughness. Three-dimensional Euler number was computed by CTAn from binarized images using a connectivity-based topological framework following the Conneulor concept (Gunderson et al., 1993). For roughness of medium structure defined as short distance autocorrelation (Di Palma et al., 2017), it was determined by smoothness parameter (ν) in a variogram analysis. To characterize the spatial covariance of the binary matrix, the Matérn model was adopted due to its flexibility, which allows for a wide range of correlation behaviors without imposing Gaussianity (Di Palma et al., 2017). Under the assumption of isotopy, the Matérn model is defined as (Matérn, 1960)

$$\gamma(\mathrm{h}) = c\left(1 - \frac{1}{2^{\nu-1}\Gamma(\nu)}\left(\frac{r}{a}\right)^{\nu} K_{\nu}\left(\frac{r}{a}\right)\right), r = |h| \geq 0 \tag{21}$$

where $\gamma(h)$ is the semi-variogram [-], c is the sill [-], a is the correlation length of semi-variogram [μm], r is the spatial distance [μm], ν is the smoothness parameter that related to the pore roughness [-], Γ is the gamma function, and K_ν is the modified Bessel function of the second kind of order ν. The fitting between the experimental variogram and the Matérn model (Eq. (21)), referred to as variogram analysis, was performed using the function based on nonlinear least square method implemented in MATLAB.

Assuming isotropy (or weak anisotropy), the microstructure within a given control volume can be adequately characterized using reduced dimensionality (Davis et al., 2011; Golovnina, 2004). Thus, rather than modeling the fully connected pore network, 2D planes were extracted from 50 randomly selected subdomains to reduce computational cost and mitigate potential spatial bias. Within each subdomain, 50 planes were randomly selected, yielding 2,500 2D planes per sand sample (S4 and SM). For each of the 2,500 planes, an experimental variogram was derived using a MATLAB script provided by Schwanghart (2025). To evaluate the assumption of isotropy and the influence of domain size, variogram analyses were conducted on XY, YZ, and XZ planes using indicator fields with dimensions of 100^3, 200^3, and 400^3 voxels. The overall pore network quantification process using variogram analysis applied in this study is visualized in Fig. A1.

https://doi.org/10.5194/egusphere-2026-3736
Preprint. Discussion started: 7 August 2026

3 Results

3.1 Comparative results of Darcy-scale analytical modelling for all sands

In this section, Darcy-scale transport quantities for all sand including Sand Mixture (SM) were comprehensively interpreted. Fig. 3 compares the measured experimental data with fitted analytical solutions. Through the fitting processes, velocity and dispersion parameters for solute and heat transport through SM were determined. Before interpreting the results, it is important to assess the fitting quality to ensure the reliability of subsequent analysis. Fig. 3a shows the best and worst fitting cases between the measured and reproduced normalized concentration data from the selected analytical model (Eq. (6)). In the worst case, a small misfit appears in the tail part particularly for the farthest sensor (L29 in Fig. 1b) from the injection point. However, the *NRMSE* for all cases was below 0.023, confirming that the analytical model accurately reproduced the normalized concentration profiles.

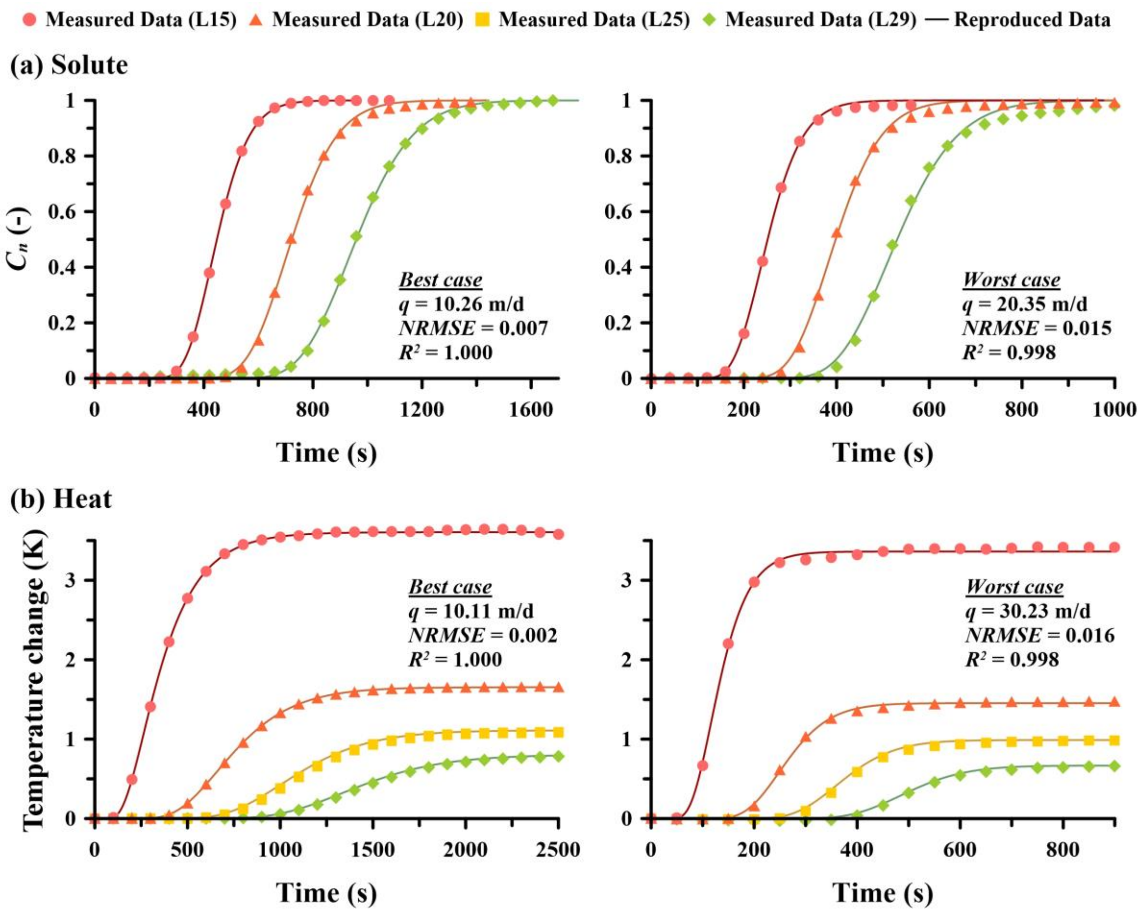

Figure 3: Examples of the best and worst fits between experimental measurements and analytical solution: (a) Best SFM results at a Darcy flux of 10.26 m/d (*NRMSE* = 0.007), and worst for a Darcy flux of 20.35 m/d (*NRMSE* = 0.015); (b) Best HFM results at a Darcy flux of 10.11 m/d (*NRMSE* = 0.002), and worst for Darcy flux of 30.23 m/d (*NRMSE* = 0.016).

https://doi.org/10.5194/egusphere-2026-3736
Preprint. Discussion started: 7 August 2026

When fitting the CPS model using Eq. (9), which describes temperature changes in a no-flow scenario dominated by thermal diffusion, the highest *NRMSE* observed was 0.080. The derived bulk thermal conductivity (λ) was 1.96 ± 0.12 W/m/K, and the bulk volumetric heat capacity (ρc) was estimated to be 2.71 ± 0.150 MJ/m³/K. These thermal properties are within the expected range for saturated sand reported by Stauffer et al. (2013). Notably, among all sand types, S5 exhibited the highest thermal conductivity and the lowest volumetric heat capacity. The thermal properties of each sand are summarized in Table 1. Based on the CPS-estimated thermal properties, the MCPS model was fitted to reproduce temperature propagation under flow scenarios (Eq. (7)). Fig. 3b provides the best and worst fitting results of the MCPS model. The *NRMSE* values consistently remained below 0.037, indicating that the selected analytical solution accurately replicated the experimental data.

Fig. 4 shows the results from the solute and heat tracer experiments, with a particular focus on front velocities and dispersion coefficients. In Fig. 4a, the estimated solute front velocities and dispersion coefficients across all experiments ranged from 8.93 to 63.02 m/d and from 3.07×10^{-7} to 3.51×10^{-6} m²/s, respectively. The averaged longitudinal solute dispersivity (α_L^s) across three locations (L15, L20, and L29) was 0.0040 m based on linear regression (R^2 = 0.769). Unlike S4 and S5, which did not exhibit a notable scale effect (Baek et al., 2022; Baek et al., 2024), the solute dispersion coefficients at L29 were higher than those at L15 and L20 when the solute front velocity exceeded 50 m/d during solute transport in SM.

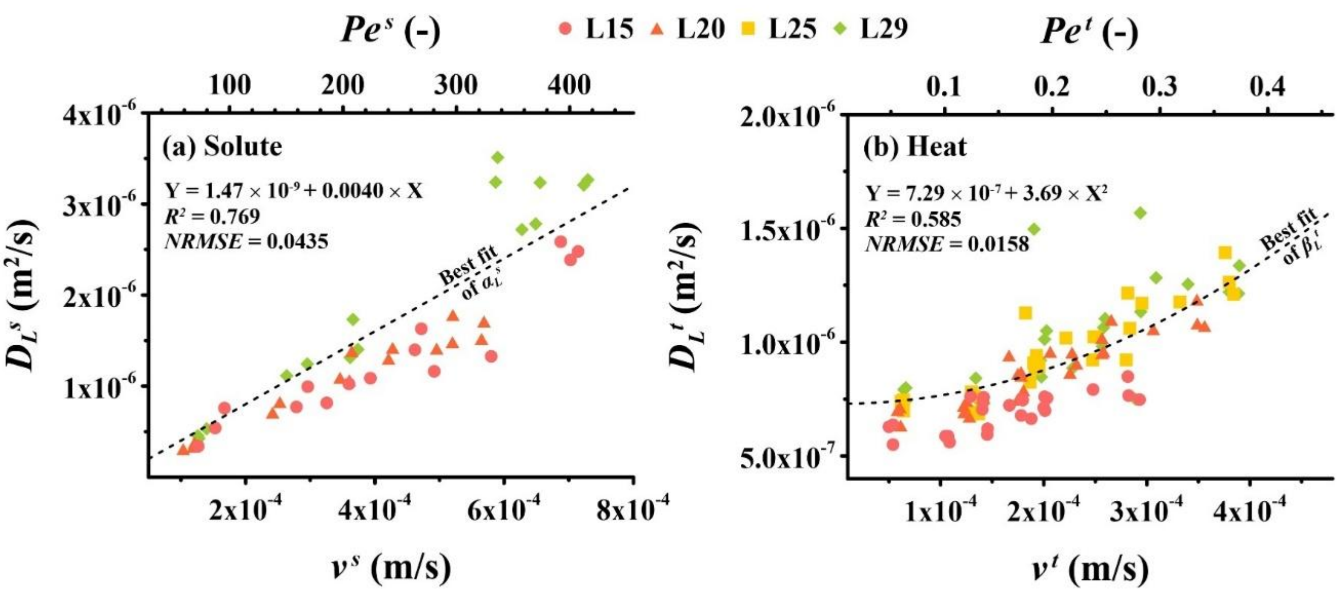

Figure 4: Estimated dispersion coefficients (Equations 3 and 9) plotted against tracer front velocities for solute (a) and heat tracer experiments (b) for SM.

https://doi.org/10.5194/egusphere-2026-3736
Preprint. Discussion started: 7 August 2026

Conversely, the estimated thermal front velocities and thermal dispersion coefficients, depicted in Fig. 4b, ranged from 4.32 to 33.66 m/d and from 5.49×10^{-7} to 1.57×10^{-6} m^2/s, respectively. These thermal parameters displayed a quadratic relationship with the longitudinal thermal dispersivity (α_L^t) of 3.69 s. The R^2 value was relatively low as 0.585, possibly due to large scatter in dispersion estimates and the low dispersion coefficient under low flow velocities. In particular, the low dispersion coefficients were smaller than the thermal diffusion coefficient (D_0^t) estimated by the CPS model. Although the CPS model reproduced the experimental data with low error, it may misestimate thermal properties by failing to capture pore-scale phenomena within a continuum-scale approach (Qu et al., 2024). Notably, for other homogeneous sands (S3, S4, and S5), such underestimation of D_0^t was not observed (Baek et al., 2024; Park et al., 2018).

For solute and heat transport in porous media, the Péclet number (Pe) helps place transport processes across different flow velocities and porous materials by incorporating tracer diffusivity and particle size, although it does not account for small-scale heterogeneity. Fig. 5 presents normalized dispersion coefficients (D_{norm}) as a function of Pe for all sands and sensor locations as well as both solute and heat. Solute dispersion coefficients were largest in the order S5 > SM > S4 at all sensor locations, while thermal dispersion coefficients showed inconsistent orders across the monitoring positions. Even with Pe normalization, differences between porous media remained clear. D_{norm} for solute showed a clear linear trend with Pe, as theoretically expected. On the other hand, that for heat displayed nonlinear increase with different trends for each sand type, consistent with Baek et al. (2024).

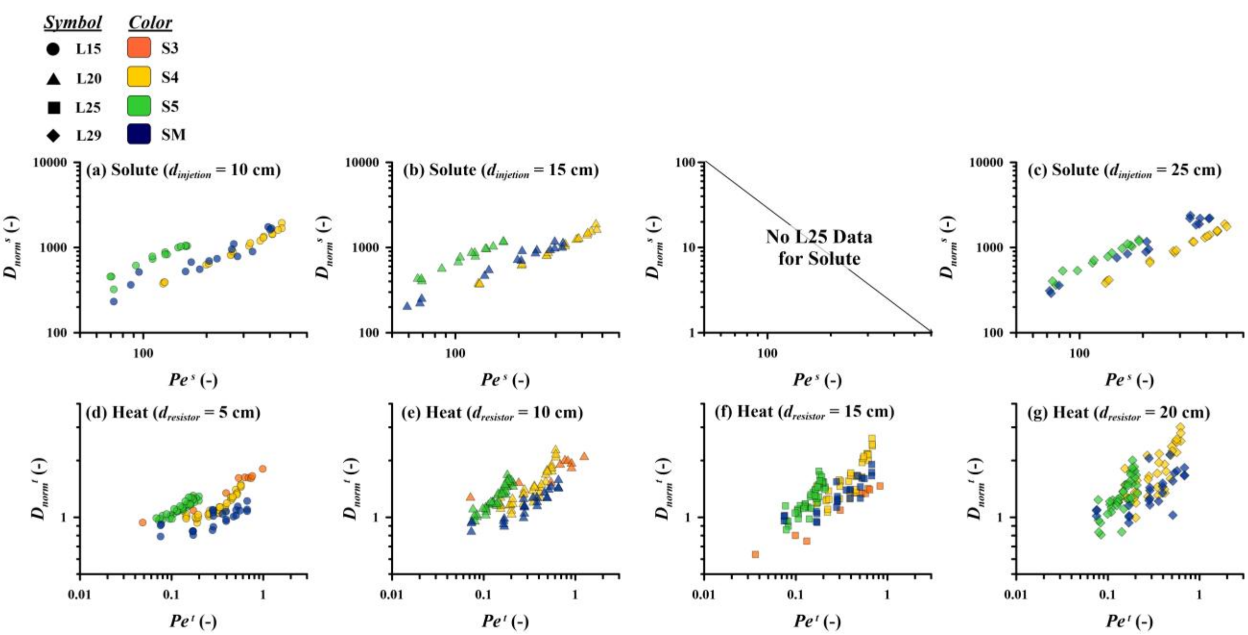

Figure 5: Normalized dispersion coefficients against Péclet number for all sand types and solute transport measured at sensor (a) L15, (b) L20, (c) L29, and for heat transport measured at sensor (d) L15, (e) L20, (f) L25, (g) L29. Data for S3 and S5 are from Park (2019).

https://doi.org/10.5194/egusphere-2026-3736
Preprint. Discussion started: 7 August 2026

3.2 Examination of bias in tracer-based Darcy fluxes

In this section, we examine the uncertainty in Darcy flux estimates derived from solute transport (q^s) by comparing them with independently measured Darcy fluxes based on volumetric flow-rate measurements ($q_{measured}$). Fig. 6a shows that the q^s estimates exhibited both over- and under-estimation, but predominantly the latter. The degree of underestimation varied by sand type with larger negative bias in S5 and SM than in S4. In addition, q^s depended on the monitoring location even under the same flow condition, indicating that spatial variability in transport behavior contributed to the variability of q^s. Interestingly, the magnitude of this spatial variability followed the same trend as the magnitude of the bias (Fig. 6a).

Unlike Darcy fluxes derived from solute data (q^s), estimating Darcy fluxes derived from heat data (q^t) additionally entails heat exchange between solid and fluid phases and thermal conduction through the solid matrix. As shown in Fig. 6b, all q^t estimates were lower than $q_{measured}$ for all experiments. The underestimation was again most pronounced in S5 and SM, consistent with the findings from the solute tracer tests. This suggests that the movement of the heat plume center in pore space can also be delayed by small-scale heterogeneity, just like for solute transport. A key difference, however, is that the underestimation of q^t relative to the measured Darcy flux was nonlinear, whereas the behavior of q^s was closer to linear with flow. The implications of these different bias patterns and their controlling mechanisms are discussed further in Sects. 4.1 and 4.2.

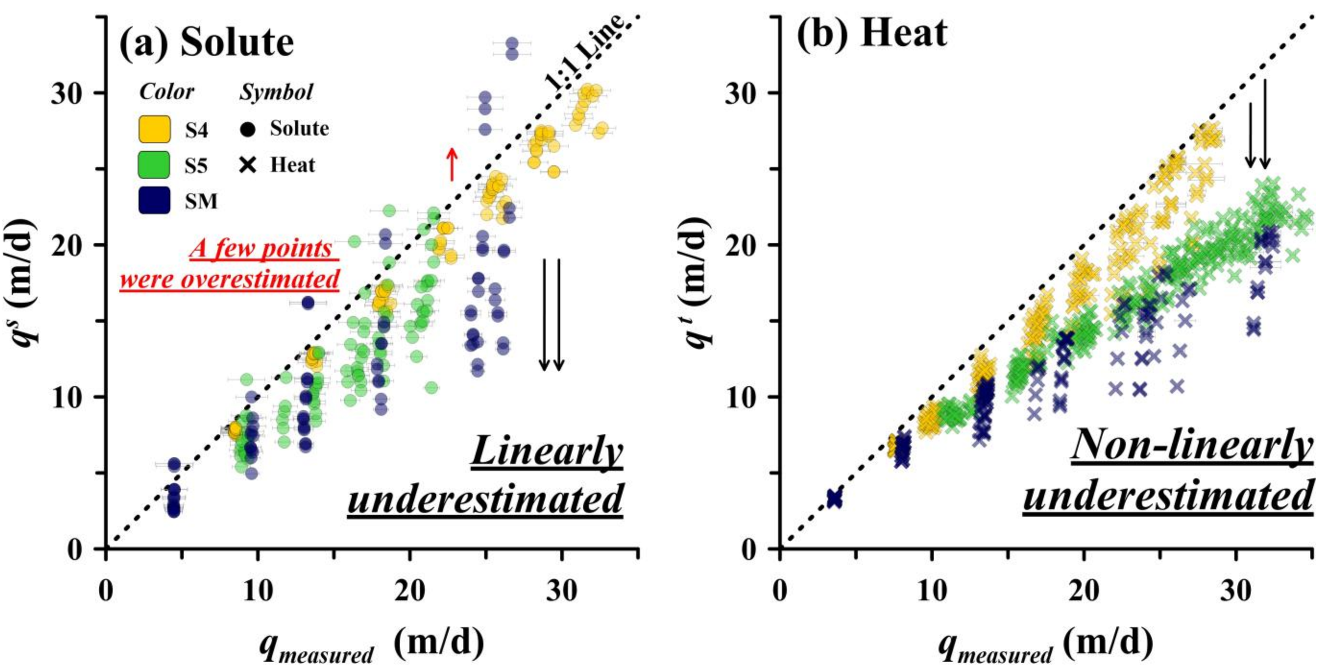

Figure 6. Darcy flux estimates from solute (a) and heat (b) transport experiments compared with the corrected Darcy flux measurements for all sands at all locations. Horizontal error bar represents the possible velocity range based on the equation (18).

https://doi.org/10.5194/egusphere-2026-3736
Preprint. Discussion started: 7 August 2026

3.3 Quantitative metrics of microstructural complexity from CT images

CT image analysis reveals clear differences in grain and pore structures between the homogeneous sand (S4) and the sand mixture (SM). Fig. 7a shows that the CT-based grain size distribution of SM was more skewed as 0.699 compared to that of S4 (0.576), similar to the results of sieve-based grain size analysis. Although the mean grain sizes derived from CT were comparable for S4 and SM (0.52 mm and 0.53 mm, respectively), both were smaller than the sieve-based means (0.76 mm and 0.84 mm, respectively). This mismatch may reflect (i) segmentation-related underestimation, (ii) sieve-related overestimation caused by irregular particle shapes, or (iii) a combination of both. The CT-based uniformity values (S4: 1.91; SM: 2.23) were higher than the sieve-based values (S4: 1.50; SM: 2.06), but the ordering (SM > S4) was preserved. The pore size distribution also shows a similar contrast (Fig. 7b). SM exhibits a skewed pore size distribution with the skewness of 0.781 and a smaller mean pore size (0.22 mm) than S4 (0.27 mm) with a slightly larger coefficient of variance (see Table 4). These features indicate a more heterogeneous pore network in SM, which is consistent with the stronger microstructural heterogeneity inferred from its grain size distribution.

https://doi.org/10.5194/egusphere-2026-3736
Preprint. Discussion started: 7 August 2026

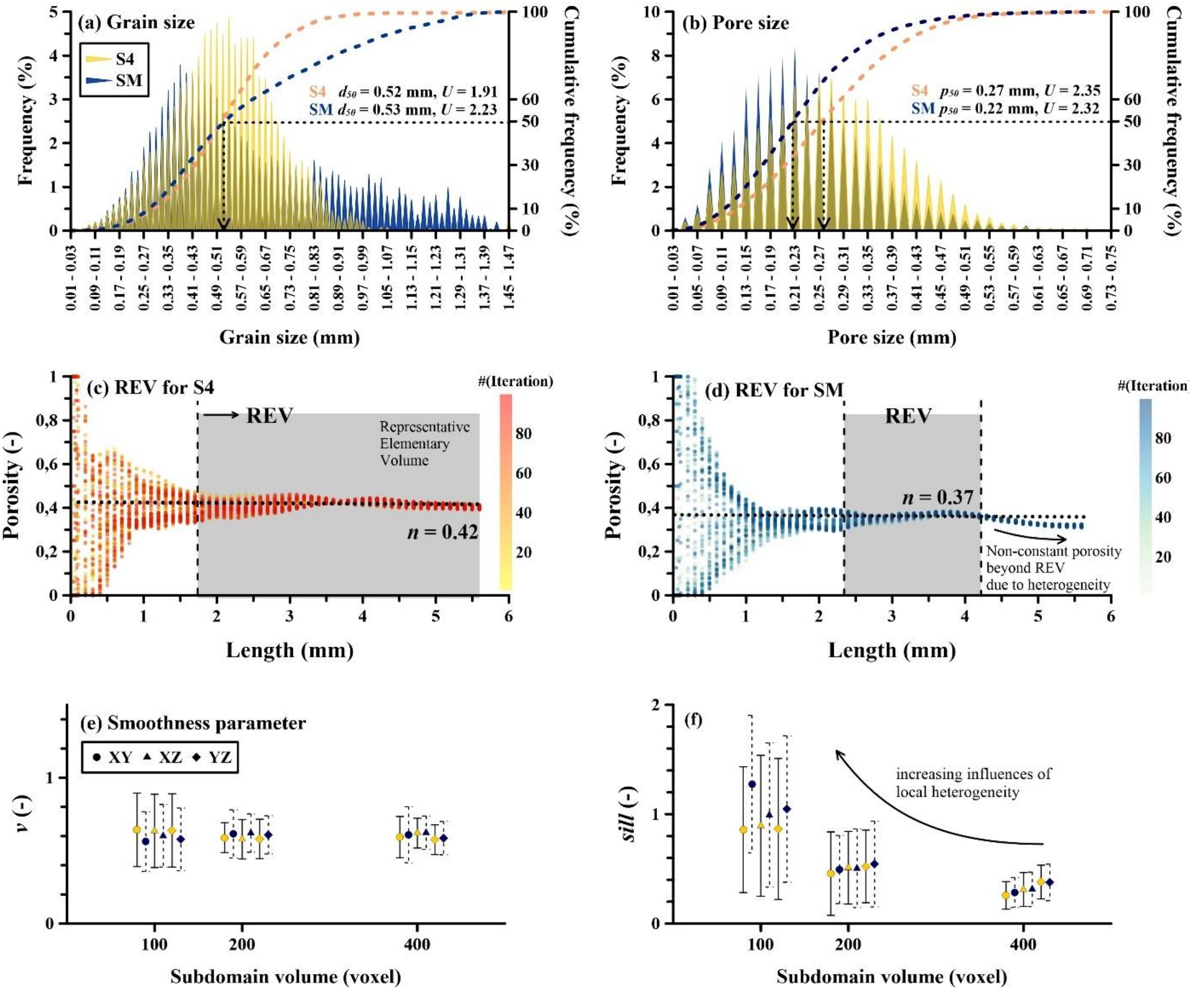

Figure 7. CT-based frequency distributions of the grain size (a), pore size (b), and porosity with respect to the representative elementary volume (REV) for S4 (c) and SM (d). Quantification of pore-structure complexity by variogram analysis results depending on subdomain volume and the direction of planes for S4 and SM. The results of Matérn model application: the smoothness parameter (e) and the sill (f).

Table 4. Statistical metrics of grain and pore size distributions obtained from CT image analysis.

Sample	Subject	Skewness	Kurtosis	Mean (mm)	CV* (-)
S4	Grain size	0.576	5.020	0.52	0.350
	Pore size	0.382	3.043	0.27	0.424
SM	Grain size	0.699	2.633	0.61	0.498
	Pore size	0.781	3.916	0.23	0.458

*CV: Coefficient of Variance (=standard deviation/mean)

https://doi.org/10.5194/egusphere-2026-3736
Preprint. Discussion started: 7 August 2026

We then estimated the representative elementary volume (REV) by computing porosity over 1,000 random sub-volumes while progressively increasing the sampled volume (Figs. 7c and 7d). For S4, the coefficient of variances of porosity were falling and remained below 10% beyond a length scale of ~1.8 mm (~180 voxel), indicating a well-defined REV. For SM, porosity exhibited a short plateau at 2.4–4.1 mm (~240–410 voxel), followed by a slow drift with increasing volume, suggesting that a larger volume is required to obtain stable bulk properties. The REV porosities were 0.42 for S4 and 0.37 for SM, slightly higher than laboratory measurements (0.37 and 0.32) but consistent in relative magnitude (S4 > SM). Overall, the agreement in trends between CT-based metrics and laboratory measurements supports the use of CT image analysis to quantify pore structures in these sands.

After the basic interpretation of CT images, the metrics representing the pore network complexity were calculated and their applicability for S4 and SM was assessed. Three-dimensional Euler numbers of S4 and SM were -6288 and -9210, respectively. Noted that the more negative Euler number means the higher degree of pore connectedness (Roque et al., 2009; Pires et al., 2020; Smet et al., 2023), indicating that SM is expected to have more complicated pore structures than S4 which is consistent with grain and pore size distributions, and REV analysis of porosity based on CT images. Figs. 7e and 7f show the variation of parameters with error bars indicating the spatial variation between selected planes within the domain. In particular, the variation of ν and sill exhibited a dependency on the subdomain volume (i.e., the size of sampled 2D plane) due to the increasing influence of local heterogeneity. Notably, the difference among XY, XZ, and YZ planes were not pronounced, supporting the validity of the isotropy assumption and suggesting that 2D variogram analysis could be representative of 3D pore structures (Davis et al., 2011). Unlike ν, the sill, the total variance of semi-variogram, was larger in SM under the subdomain of 100 voxels. However, after 200 voxels, both sill values and difference between S4 and SM were decreased. This means that SM was more heterogeneous than S4 in 100-voxel scale, but those small heterogeneities were averaged when subdomain was larger than 200 voxels. While direct metrics from CT images suggest that SM had a more complex pore network, the Matérn model parameter ν, an indirect indicator of pore roughness suggested by Di Palma et al. (2017), did not differ significantly between the two sands.

3.4: Synthesis of microstructural metrics and tracer bias

To test whether the microstructural contrasts revealed by CT imaging account for the divergent tracer behaviors reported in Sects. 3.1–3.2, we compared the two scanned endmembers—S4 and SM—under the constraint that their mean grain sizes are nearly identical (d_{50} = 0.76 mm vs. 0.84 mm) while their grain-size uniformity differs markedly (U = 1.50 vs. 2.06). This pairing isolates pore-network complexity from grain-size effects.

For solute transport, the CT-derived pore-size distribution of SM is more right-skewed (0.781) and more variable (CV = 0.458) than that of S4 (skewness = 0.382, CV = 0.424; Table 4). These structural differences parallel the observed breakthrough-curve statistics: EC time series for SM are more right-skewed than those for S4 (Fig. A2), and the degree of right-skewness in the BTCs increases systematically from S4 → S5 → SM (Figs. 8c, and d). The sands with stronger breakthrough skewness

https://doi.org/10.5194/egusphere-2026-3736
Preprint. Discussion started: 7 August 2026

(S5 and SM) also exhibit the largest linear underestimation of q^s (Fig. 6a), reaching ~25% in SM versus <10% in S4. This directional consistency suggests that a wider, skewed pore-size spectrum creates preferential flow pathways and stagnant pore zones that delay the solute front, producing the systematic negative bias captured by the Darcy-scale model.

For heat transport, the contrast is sharper. SM possesses a more negative Euler number (−9,210) than S4 (−6,288), indicating a higher degree of pore connectedness and more complex pore structure (Sect. 3.3), and its porosity fails to stabilize beyond the pseudo-REV plateau at 2.4–4.1 mm (Fig. 7d). These structural features coincide with two macroscopic heat-transport symptoms that are absent in S4. First, SM exhibits anomalous thermal dispersion: its fitted thermal dispersion coefficients fall below the no-flow thermal diffusion coefficient estimated by the CPS model (Fig. 4b), a phenomenon not observed in the homogeneous sands (S3, S4, S5). Second, SM produces a nonlinear, velocity-dependent underestimation of q^t that reaches ~45% (even after accounting for 19% spatial variability in volumetric heat capacity, Table 1) at the highest tested velocity, whereas S4 remains within 10–20% (Fig. 6b). The divergence between solute- and heat-derived flux estimates, quantified by the ratio $q^s/q^t = R_{eff}/R_{app}$ (Eq. (15)), increases with flow velocity for SM but remains near unity for S4 (Fig. 9m–o). This pattern is consistent with the hypothesis that SM's tortuous, highly connected microstructure disrupts solid-phase conduction and reduces effective interphase heat transfer, amplifying local thermal non-equilibrium under fast flow.

Collectively, the controlled S4–SM comparison indicates that the CT-derived metrics—pore-size skewness, Euler number, and REV instability—directionally predict the magnitude and the tracer-specific signature of Darcy-flux bias. Where S4's relatively homogeneous, well-connected pore network yields similar solute and heat flux estimates, SM's complex microstructure generates the linear solute retardation and the nonlinear heat retardation that together define the outlier behavior of the sand mixture in the four-sand transport trend.

https://doi.org/10.5194/egusphere-2026-3736
Preprint. Discussion started: 7 August 2026

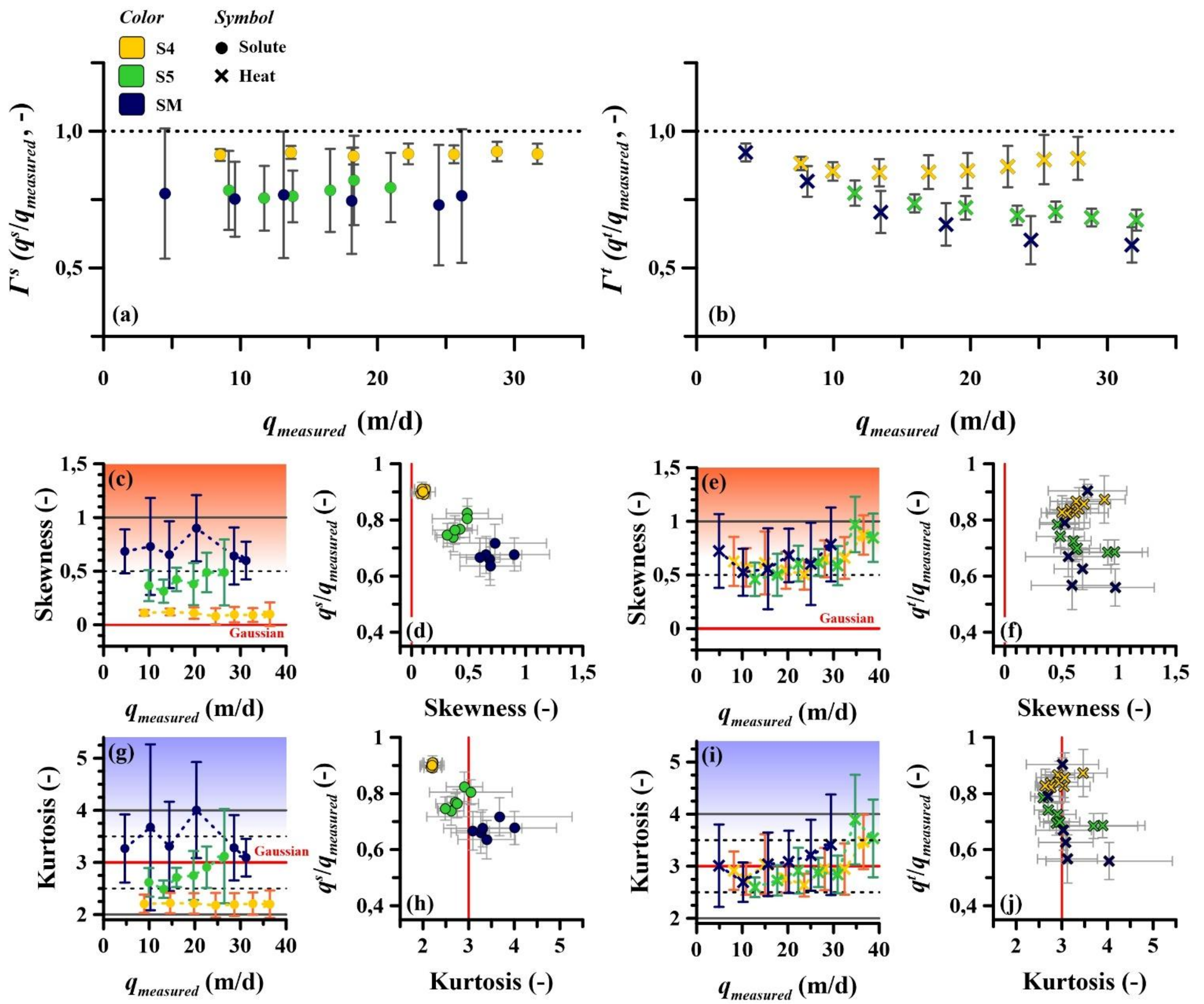

Figure 8. Comparison of solute- (a) and heat-based (b) Darcy flux estimates to measured Darcy flux and statistical characteristics of EC (c,d,g,h) or temperature time-series (e,f,i,j) for different sand types (S4: yellow. S5: green, and SM: navy). Panels (c,g) show the dependence of skewness and kurtosis for EC data on flow velocity and (d,h) their relationships with solute-based Darcy flux underestimation, while panels (e,f,i,j) present the corresponding results for temperature data (heat tracer). The red solid line indicates perfect Gaussian. Symbols in panels (c–j) represent the mean values for each flow velocity, based on all monitoring points and replicate experiments, and error bars denote one standard deviation.

https://doi.org/10.5194/egusphere-2026-3736
Preprint. Discussion started: 7 August 2026

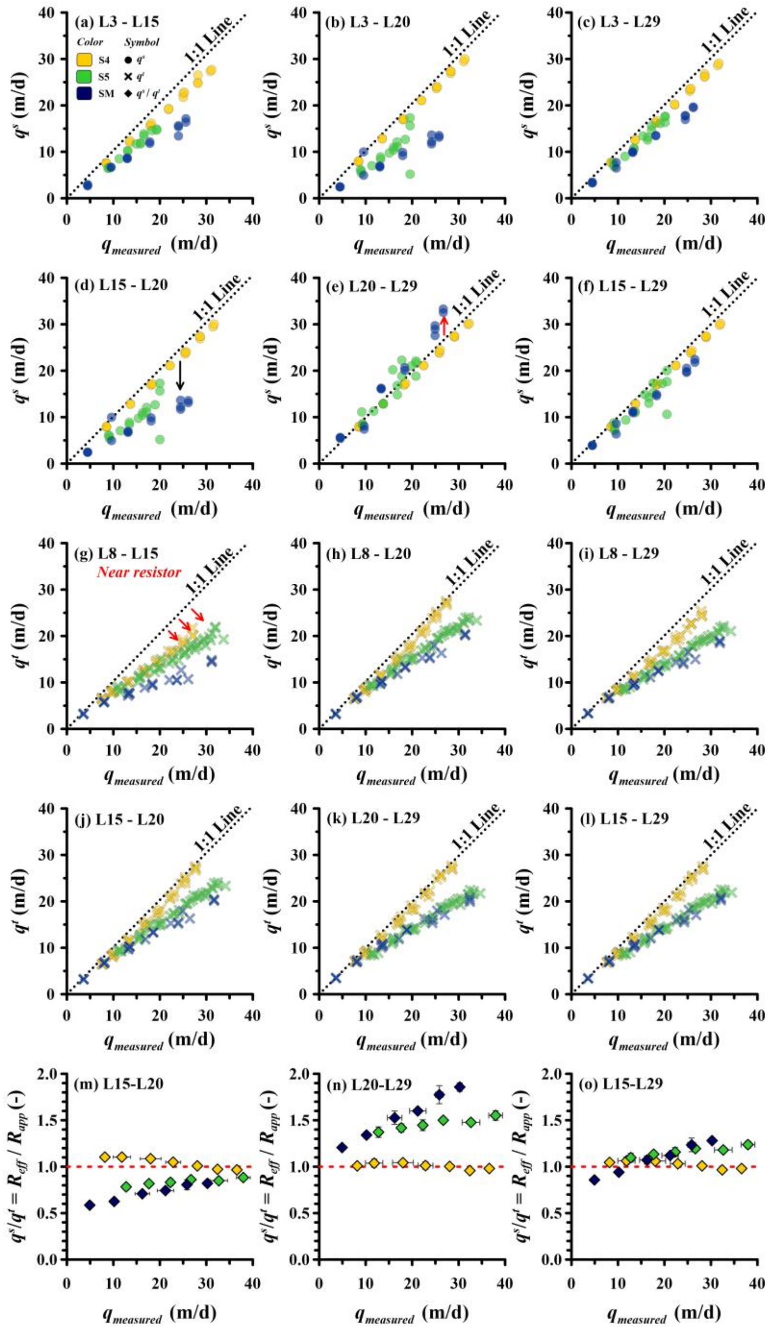

Figure 9. Darcy flux estimates from solute (a–f) and heat (g–l) compares with the corrected Darcy flux measurements for all sands at L15 (a and g), at L20 (b and h), at L29 (c and i), at interval of L15 and L20 (d and j), at interval of L20 and L29 (e and k), at interval of L15 and L29 (f and l). The ratio between Darcy flux estimates from solute (q^s) and heat (q^t) was only calculated for the same representative intervals of L15–L20 (m), L20–L29 (n), L15–L29 (o). Noted that q^s/q^t is identical to R_{eff}/R_{app} as described in equation (14). Error bars in (m–o) indicate the variation across replicated experiments conducted under similar flow velocities.

https://doi.org/10.5194/egusphere-2026-3736
Preprint. Discussion started: 7 August 2026

4 Discussion

4.1 Divergent tracer-specific bias regimes

The central finding of this study is that identical microstructures produce fundamentally different, physics-dependent systematic biases in Darcy-flux estimation depending on tracer type. For solute transport, the underestimation of q^s scaled approximately linearly with $q_{measured}$ across the tested velocity range ($R^2 > 0.95$; Fig. 6a), with the degree of bias varying by sand type: on average, q^s was underestimated by ~25% in S5 and SM, whereas the underestimation remained below 10% in S4. For heat transport, all q^t estimates were lower than $q_{measured}$, but the pattern was markedly nonlinear (Fig. 6b). In the most heterogeneous medium (SM), heat-based Darcy fluxes were underestimated by up to 45% (including 19% uncertainty from spatial variability in volumetric heat capacity; Table 1) at the highest tested velocity (~32 m/d), whereas S4 remained within 10–20% underestimation even at comparable flow rates.

The divergence is captured quantitatively by the effective-to-apparent retardation ratio ($q^s/q^t = R_{eff}/R_{app}$; Eq. (15)). For S4, this ratio remained near unity across all flow velocities and monitoring intervals (Fig. 9m–o), indicating that solute and heat tracers yielded effectively equivalent flux estimates in the relatively homogeneous sand. For SM, however, the ratio increased systematically with flow velocity, reaching values substantially greater than 1.0 at the highest velocities (Fig. 9m–o). This velocity-dependent decoupling demonstrates that the two tracers are not interchangeable proxies for groundwater flow in heterogeneous media; rather, they sample different ensemble averages of the same pore-scale velocity field, filtered through distinct physics (advection–dispersion for solute versus advection–conduction–interphase exchange for heat).

An important caveat is that the measured Darcy flux may carry systematic uncertainty due to preferential flow along the tank walls or outlet discharge measurement error. If such effects are present, they would inflate the apparent tracer bias. However, three lines of evidence suggest that the observed patterns are not dominated by experimental artifact. First, S4 - the most homogeneous sand with a stable REV and near-Gaussian pore-size distribution - exhibits a baseline bias of ~10 % for solute and ~10–20 % for heat, with $q^s/q^t \approx 1$ across all velocities (Fig. 9m–o). This baseline likely represents the upper bound of systematic experimental error in our setup. Second, the more heterogeneous sands (S5 and SM) show substantially larger bias (~25 % for solute, up to ~45 % for heat), and the divergence between solute and heat increases with velocity for SM. A uniform wall effect or measurement error would not produce this tracer-specific, sand-dependent divergence. Third, the bias scales linearly with $q_{measured}$ for each sand ($R^2 > 0.95$), consistent with a constant structural retardation factor rather than random noise. We therefore interpret the excess bias beyond the S4 baseline as the true signature of microstructural heterogeneity, while acknowledging that the absolute bias magnitudes may be modestly inflated by unavoidable experimental uncertainty.

These findings align with the comparative assessment of Irvine et al. (2015), who noted that heat and solute tracers perform differently in heterogeneous aquifers. However, our controlled experiments extend that observation by isolating the mechanism: the divergence is not merely a product of macroscopic hydraulic conductivity contrasts, but arises from microstructural complexity that is invisible to standard grain-size statistics. The S4 versus SM endmember pair—matched in mean grain size ($d_{50} \approx 0.76$–0.84 mm) but divergent in pore-network complexity (Euler number, pore-size skewness, and REV stability; Table

https://doi.org/10.5194/egusphere-2026-3736
Preprint. Discussion started: 7 August 2026

4, Fig. 7)—provides the structural explanation for why SM breaks the homogeneous-sand trend established by S3, S4, and S5. Where S4's relatively uniform, Gaussian-like pore-size distribution and stable REV yield tracer estimates that converge, SM's skewed, heterogeneous microstructure generates the linear solute retardation and the nonlinear heat retardation that together define its outlier behavior.

4.2 Microstructural controls on solute transport: from pore-size skewness to non-Gaussian breakthrough

The CT-derived pore-size distributions reveal a clear structural basis for the observed solute transport bias. SM exhibits a more right-skewed pore-size distribution (skewness = 0.781) and a larger coefficient of variation (CV = 0.458) than S4 (skewness = 0.382, CV = 0.424; Table 4), despite their comparable mean grain sizes. This wider, asymmetric pore-size spectrum creates a broad distribution of pore-scale velocities: larger pore throats act as preferential channels where solute advances rapidly, while smaller pores and dead-end regions retard transport through slow advection and diffusion. The net effect is a partitioning of the solute plume across disparate velocity classes, which manifests macroscopically as right-skewed, non-Gaussian breakthrough curves (Figs. 8c, 8d and A2).

This structural–transport linkage is supported by the systematic trend across all four sands. EC breakthrough curves became increasingly right-skewed from S4 to S5 and SM, and the sands with stronger breakthrough skewness (S5 and SM) also exhibited the largest negative bias in q^s (Fig. 6a). Importantly, both skewness and kurtosis varied primarily across sand types and showed little dependence on flow velocity (Figs. 8c and 8g), indicating that the bias originates from static structural controls rather than from changes in the imposed flow conditions. Over the tested range of flow velocities, q^s scaled approximately linearly with $q_{measured}$ ($R^2 > 0.95$; Fig. 6a), implying that the ratio Γ^s ($= q^s/q_{measured}$; Eq. (20))remained nearly constant for each sand. On average, q^s was underestimated by ~25% in S5 and SM, whereas the underestimation remained below 10% in S4.

Non-Gaussian breakthrough behavior can arise from pore-scale complexity through heterogeneous permeability and pre-asymptotic dispersion, including chaotic advection within pore spaces (Dentz et al., 2023). Field studies have similarly shown that subsurface heterogeneity delays the migration of the solute plume center of mass through irregular plume geometry and pronounced tailing, ultimately leading to underestimation of q^s when inferred from front velocity or breakthrough timing (Freyberg, 1986; Gelhar et al., 1992; Zech et al., 2021). Numerical results by Di Palma et al. (2017) likewise demonstrated a systematic decrease of solute front velocity with increasing pore-network complexity. In our CT analysis, SM is expected to have a more complex pore network relative to S4 (Fig. 7) with a more negative Euler number (−9,210 versus −6,288), and q^s estimates for SM indeed illustrated greater underestimation. This finding reinforces the hypothesis that microstructural heterogeneity intensifies small-scale velocity variations and delays the effective transport front, thereby leading to the buildup of systematic errors in Darcy-scale flux estimates.

https://doi.org/10.5194/egusphere-2026-3736
Preprint. Discussion started: 7 August 2026

At the same time, such inference requires caution when relying only on time-series data from a single monitoring point (Sole-Mari et al., 2021). Within these limitations, our results indicate that even subtle, sand-dependent departures from Gaussian breakthrough behavior—quantifiable through the skewness of the pore-size distribution itself—can introduce a systematic negative bias in solute-derived Darcy flux estimates under Darcy-flow conditions. Recognizing and diagnosing such non-Gaussian features, and linking them directly to CT-derived metrics of pore-network shape, should therefore be treated as a necessary step when interpreting tracer tests in natural porous media.

4.3 Microstructural controls on heat transport: LTNE amplified by pore-network connectivity

Although solute and heat tracers were tested under identical flow conditions, the resulting Darcy flux estimates behaved differently. Solute-derived Darcy fluxes (q^s) showed a largely systematic underestimation associated with deviations from Gaussianity in EC breakthrough curves, whereas heat-derived fluxes (q^t) exhibited stronger nonlinearity and less consistent links to the temperature time-series statistics (Fig. 8). For EC, skewness and kurtosis separated clearly by sand type, but for temperature the corresponding statistics overlapped substantially across sands. The location of maximum skewness also differed between tracers: temperature skewness peaked at the closest monitoring point (L15), whereas EC skewness for solute transport was largest at the farthest sensor (L29) for all sands (Fig. A2). Consistently, Γ^t ($=q^t/q_{measured}$; Eq. (20)) varied nonlinearly with flow velocity for SM and S5 (but not for S4), and temperature skewness and kurtosis exhibited an abrupt change around 25–30 m/d (Figs. 8b, 8e and 8i). Moreover, the magnitude of q^t underestimation was not simply explained by skewness; for example, S4 reached skewness values near 1 while q^t remained within 10–20% underestimation, whereas SM showed the largest underestimation, approaching 45% at the highest tested velocity (~32 m/d). Even with spatial variability of volumetric heat capacity represented by a standard deviation (19%, see Table 1), the maximum underestimation of heat-based Darcy flux is more noticeable than solute-based under the highest flow velocity condition.

The strongest q^t underestimation occurred between L8 and L15 across all sands, and in many cases exceeded the underestimation observed for q^s. A potential explanation for this localized behavior is buoyancy-induced flow, but our conditions suggest this is unlikely. The maximum temperature difference between L8 and L15 was 5–23 K, well below the estimated threshold for the onset of pure natural convection ($\Delta T \approx 47$ K for Rayleigh number >27), calculated following Raffensperger and Vlassopoulos (1999) and de Marsily (1986). In addition, the underestimation increased with flow velocity, whereas buoyant effects would be expected to diminish under stronger forced flow. The fact that q^t approached $q_{measured}$ at low velocities provides additional support that buoyancy is not the dominant control.

A more plausible mechanism is that heat transport is affected by additional micro-scale processes absent in solute transport, including conduction through the solid matrix and incomplete thermal equilibration between solid and fluid phases (also known as LTNE). When solid conduction and/or interphase heat transfer are not sufficiently fast relative to advection, the apparent thermal front can become delayed and more diffuse, which biases q^t inferred from front migration (Qu et al., 2024). The CT-derived microstructure of SM provides the geometric basis for this delay. SM possesses a more negative Euler number (−9,210)

https://doi.org/10.5194/egusphere-2026-3736
Preprint. Discussion started: 7 August 2026

than S4 (−6,288), indicating a higher degree of pore connectedness and more complex pore structure (Sect. 3.3), and its porosity fails to stabilize beyond the pseudo-REV plateau at 2.4–4.1 mm (Fig. 7d). These structural features imply a tortuous, highly connected pore network that disrupts effective local solid-conduction pathways and enhances spatial variability in thermal exchange, analogous to the role of heterogeneity in solute transport (Ghanbarian and Daigle, 2016; Yang and Nakayama, 2010). Because L8 marks the resistor location, the L8–L15 segment experiences the strongest and most rapidly evolving temperature gradients, making it especially sensitive to LTNE and microstructural controls. Accordingly, SM exhibited substantially stronger q^t underestimation in the L8–L15 segment than S4 (Fig. 9g).

Roshan et al. (2014) similarly emphasized that LTNE can bias heat-based Darcy flux estimates at low velocities, as the thickening of the thermal boundary layer impedes efficient heat transfer between the solid matrix and the adjacent fluid. Conversely, Gossler et al. (2020) argued that advective thermal velocities remain unaffected, and Gebhardt et al. (2025) agreed with this finding only under homogeneous conditions. Under heterogeneous hydraulic conductivity, however, the effective retardation factor defined as Eq. (16), deviated from theoretical apparent retardation factor (Eq. (17))—referred to as field-scale LTNE in Gebhardt et al. (2025). Interestingly, our results also aligned with their macro-scale findings: S4 (more homogeneous) produced similar q^s and q^t estimates, whereas SM (more heterogeneous) showed increasing divergence between solute- and heat-based flux estimates as flow velocity increased (Figs. 9m–9o). This divergence is also consistent with CT-derived microstructural indicators such as three-dimensional Euler number.

Overall, the influence of microstructural heterogeneity on heat-based Darcy flux estimation is flow-velocity dependent, and the changing balance among advection, dispersion, and conduction with increasing velocity can produce nonlinear q^t behavior. These findings emphasize that micro-scale processes (e.g., LTNE and differential conduction) can be a dominant source of bias in heat-tracer interpretation, particularly under relatively fast groundwater flow.

4.4 Implications for upscaling metrics and tracer selection

The findings of this study demonstrate that microstructural heterogeneity arising from different grain texture or pore structure can significantly influence Darcy-scale interpretations for both solute and heat transport, leading to errors in Darcy flux estimation. In particular, our results agreed with Irvine et al. (2015) that in regions with relatively low groundwater velocities, heat tracers—being less sensitive to small-scale structural variations—may serve as a more suitable proxy than solute tracers for estimating the average Darcy flux. However, the onset of LTNE under higher flow conditions can be exacerbated by pore-scale complexity and may cause systematic underestimation of q^t. LTNE not only affects the migration of the thermal plume center but may also distort the estimation of thermal properties, further complicating thermal flux interpretation. Unfortunately, the potential for misestimating thermal properties due to LTNE remains poorly understood, particularly its dependence on flow velocity, from an experimental perspective. Given the lack of prior studies, further investigation is needed to explore how LTNE interferes with Darcy-scale heat transport behaviors as a function of micro-scale properties such as pore roughness and connectedness.

https://doi.org/10.5194/egusphere-2026-3736
Preprint. Discussion started: 7 August 2026

Our findings underscore that conventional parameter-inverse approaches may mischaracterize both flux and conductivity in natural settings. The occurrence of LTNE further complicates the interpretation of thermal transport, highlighting the nonlinear and scale-dependent role of pore structural complexity. However, existing metrics representing pore roughness to bridge micro-scale pore structure and Darcy-scale transport cannot fully explain our experimental results. Although S4 and SM had similar v values (Fig. 7e), their grain and pore size distributions were markedly distinct (Figs. 7a and 7b). The sill was meaningfully larger in SM only under 100-voxel scale, indicating the importance of assigning REV to derive the pore-representative metric. Darcy-scale transport analyses further highlighted the distinctive behavior between S4 and SM for both solute and heat tracers. Without an adequate metric, the influence of local geometric variability within the pore space will likely continue to be overlooked or attributed to model uncertainty in Darcy-scale interpretations.

To feasibly incorporate complex micro-scale structures into simple Darcy-scale modeling frameworks, a better metric that robustly quantifies pore network complexity is urgently needed. Such a metric should link microstructural characteristics—such as pore-size distribution skewness, Euler number, and REV stability—with measurable deviations in macroscopic transport behavior, including non-Gaussian breakthrough and tracer-specific flux bias. Introducing such a metric would not only enhance the predictive accuracy of flow and heat transport models, but also offer a practical tool for identifying regimes in which pore-scale effects are non-negligible. These findings further emphasize the importance of developing multi-scale modeling frameworks that explicitly integrate pore-scale heterogeneity into continuum-scale analyses. Such integration will improve the reliability of solute and heat-based tracing in heterogeneous aquifers and guide the design of future experiments aimed at quantifying LTNE effects under realistic flow conditions. For more effective multi-scale interpretations, future work should integrate refined upscaling techniques with advanced quantitative metrics that robustly link matrix microstructure to macro-scale properties. Such approaches would improve the accuracy and reliability of continuum-scale transport models, especially in naturally heterogeneous systems, and support better-informed hydrogeological decision-making in both research and applied contexts.

5 Conclusion

We conducted a series of heat and solute tracer experiments using four different sands that span distinct grain- and pore-size distributions to investigate how microstructural heterogeneity influences the estimation of transport parameters at the Darcy scale. Pore and grain structures for two sands were captured via micro-CT and analyzed using topological and geostatistical methods. Tracer injection was monitored at four monitoring points with 5-cm interval, and observed time series of EC and temperature closely matched analytical solutions (mean $R^2 > 0.99$ and NRMSE < 0.037), confirming that the adopted Darcy-scale modeling approach is internally consistent. However, the high quality of model fits masked a systematic, tracer-specific divergence in flux estimation that is invisible to standard goodness-of-fit criteria.

https://doi.org/10.5194/egusphere-2026-3736
Preprint. Discussion started: 7 August 2026

The central finding is that identical microstructures produce fundamentally different bias regimes depending on tracer physics. For solute transport, Darcy fluxes were linearly underestimated by ~25% in the more heterogeneous sands (S5 and SM) and by <10% in the relatively homogeneous S4. This linear bias was directionally linked to the skewness of the pore-size distribution: SM's more right-skewed, higher-CV pore network (skewness = 0.781, CV = 0.458 versus S4's 0.382 and 0.424) generated non-Gaussian, right-skewed breakthrough curves that reflect preferential flow partitioning and stagnant-zone retention, systematically delaying the inferred solute front. For heat transport, the underestimation was nonlinear and velocity-dependent, reaching up to 45% (including 19% uncertainty from spatial variability in thermal properties) in SM at the highest tested velocity (~32 m/d), whereas S4 remained within 10–20%. This nonlinear retardation was consistent with local thermal non-equilibrium (LTNE) amplified by SM's more complex pore structure, as evidenced by its more negative Euler number (−9,210 versus −6,288 for S4) and its failure to reach a stable representative elementary volume within the tested CT volume. The resulting divergence between solute- and heat-derived flux estimates ($q^{s}/q^{t} = R_{eff} / R_{app}$; Eq. (15)) increased with flow velocity for SM but remained near unity for S4, demonstrating that the two tracers sample different ensemble averages of the same pore-scale velocity field.

These results carry practical implications for tracer-based hydrogeological characterization. Heat tracers may serve as a more suitable proxy than solute tracers for estimating average Darcy flux under relatively low groundwater velocities in homogeneous media, where LTNE is negligible. However, they become less reliable under high-velocity conditions in heterogeneous media, where pore-network complexity exacerbates LTNE and causes systematic underestimation. Recognizing non-Gaussian breakthrough behavior - quantifiable through skewness and kurtosis of tracer time series - as a macroscopic fingerprint of sub-REV structural complexity should become a standard diagnostic step before interpreting flux estimates.

Methodologically, this study demonstrates that conventional descriptors such as mean grain size and uniformity coefficient, as well as standard geostatistical metrics such as the Matérn smoothness parameter, are insufficient to predict the observed transport divergence. The controlled S4–SM endmember pair, matched in mean grain size but divergent in pore-network complexity, reveals that process-aware metrics drawn from high-resolution micro-CT—including pore-size distribution skewness, Euler number, and REV stability—are needed to bridge pore-scale structure to Darcy-scale transport behavior. Future work should integrate these refined quantitative metrics into multi-scale modeling frameworks that explicitly account for how microstructural heterogeneity activates distinct physical processes (non-Gaussian mechanical dispersion versus LTNE) for different tracers. Such integration will improve the reliability of solute- and heat-based tracing in naturally heterogeneous aquifers and guide the design of experiments aimed at quantifying LTNE effects under realistic flow conditions.

https://doi.org/10.5194/egusphere-2026-3736
Preprint. Discussion started: 7 August 2026

Appendix A

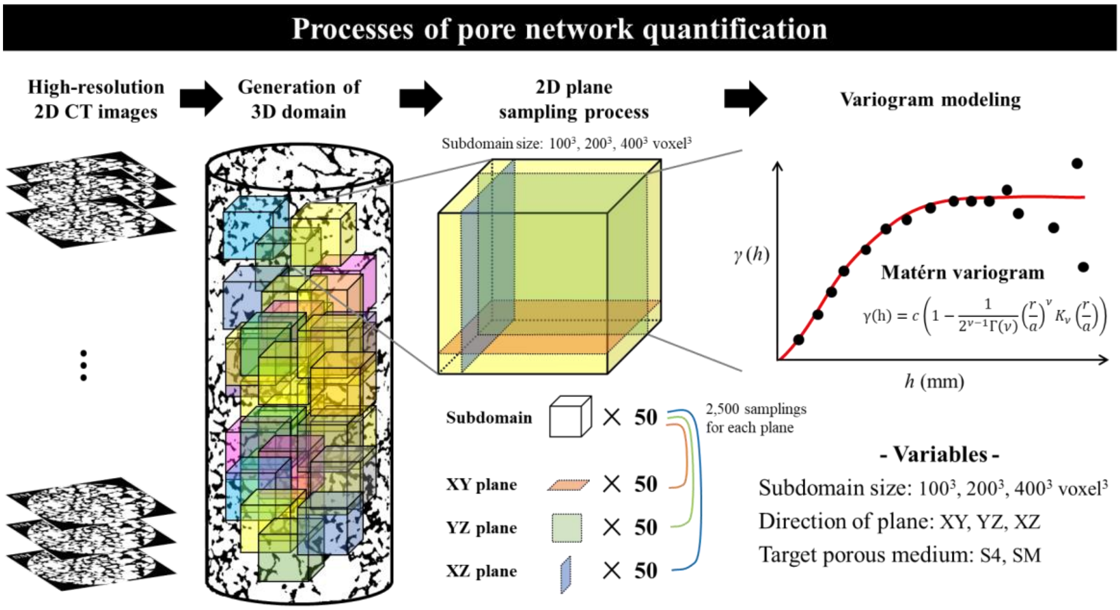

655 **Figure A1. Schematic diagram visualizing the microstructural complexity examination process applied to sand samples used in the current study.**

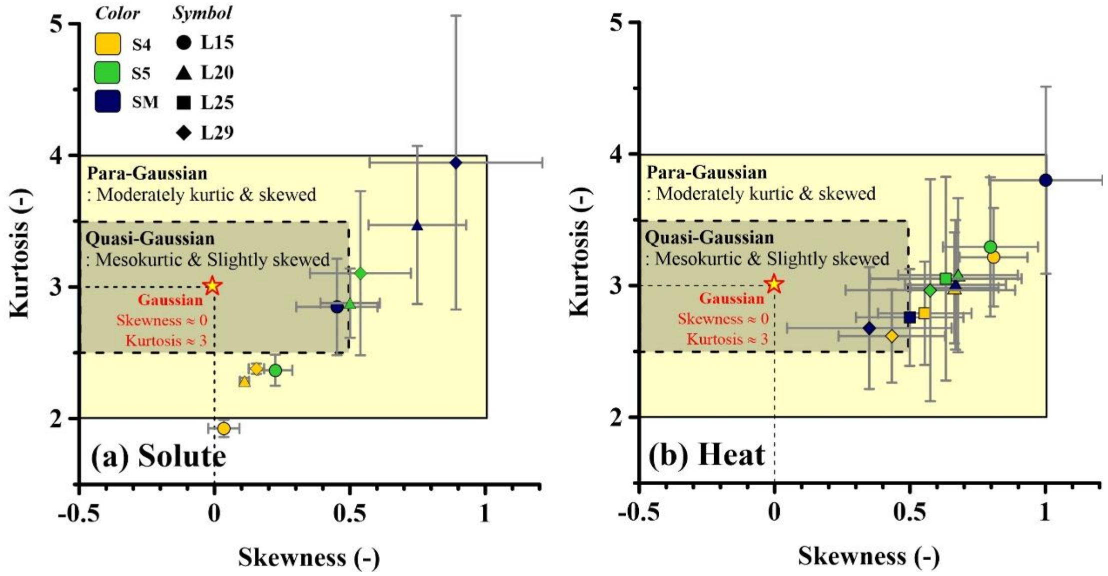

660 **Figure A2. Statistical evaluation of obtained fluid EC (a) and temperature (b) time series depending on different sand types (S4, S5, and SM) via skewness (x-axis) and kurtosis (y-axis). Joint distribution of skewness and kurtosis illustrating the normality of each experiment across the monitoring locations (L15, L20, and L29). Error bars indicate the standard deviations across all velocities and repeated experiments. The shaded box highlights the Quasi-Gaussian regime (Mesokurtic and slightly skewed) and the Para-Gaussian (Moderately kurtic and skewed), while the star symbol indicates the ideal Gaussian condition (Skewness = 0, and Kurtosis = 3). Color and symbol legends represent the sand types and monitoring locations.**

https://doi.org/10.5194/egusphere-2026-3736
Preprint. Discussion started: 7 August 2026

Code and data availability

The data required to reproduce the results, figures, and tables presented in this manuscript are currently available to reviewers through the Copernicus review system with restricted access. Upon acceptance and before final publication, the experimental data, and micro-CT data will be deposited in a FAIR-aligned public data repository, such as Figshare, and will be made publicly available with a DOI. No third-party data were used in this study.

Author contributions

Ji-Young Baek and Gabriel Rau conceptualized the study and developed the methodology. Ji-Young Baek and Byeong-Hak Park conducted the formal analysis, performed validation. Ji-Young Baek developed the software, curated data and performed visualization. Ji-Young Baek, Byeong-Hak Park and Gabriel Rau conducted the investigation and prepared the original draft of the manuscript. Kang-Kun Lee acquired funding, administered the project, provided resources, and supervised the work.

Competing interests

At least one of the co-authors is a member of the editorial board of Hydrology and Earth System Sciences.

Disclaimer

No additional disclaimer is needed.

Acknowledgements

The authors would like to express their sincere gratitude to colleagues (Hae-Rim Oh, Yeji Kim, Dr. Seung-Wook Ha) who provided valuable support in setting the experimental apparatus used in this study. We are also deeply grateful to Prof. Sung Keun Lee, whose insightful comments enhanced the quality of this work.

Financial support

This work was supported by the National Research Foundation of Korea (NRF) grant funded by the Korea government (MSIP and MSIT) (No. 2022R1A2C1006696 and No. RS-2022-NR070842). This work was also supported by the Institute for Korea Spent Nuclear Fuel (iKSNF) and the National Research Foundation of Korea (NRF) grant funded by the Korean government (Ministry of Science and ICT, MSIT) (No. RS-2021-NR056203).

https://doi.org/10.5194/egusphere-2026-3736
Preprint. Discussion started: 7 August 2026

References

Afshari, S., Hejazi, S.H., and Kantzas, A.: Pore-scale modeling of coupled thermal and solutal dispersion in double diffusive-advective flows through porous media. Int. J. Heat Mass Transf. 147, 118730. https://doi.org/10.1016/j.ijheatmasstransfer.2019.118730, 2020.

Anderson, M. P.: Heat as a ground water tracer. Groundwater, *43*(6), 951-968, https://doi.org/10.1111/j.1745-6584.2005.00052.xDigital Object Identifier (DOI), 2005.

Baek, J.Y., Park, B.H., Rau, G.C., and Lee, K.K.: Experimental evidence for local thermal non-equilibrium during heat transport in sand representative of natural conditions. J. Hydrol. 608, 127589. https://doi.org/10.1016/J.JHYDROL.2022.127589, 2022.

Baek, J.Y., Park, B.H., Rau, G.C., and Lee, K.K.: Experiments reveal effects of particle and pore-scale heterogeneity on thermal dispersion during porous media heat transport. J. Hydrol. 639, 131568. https://doi.org/10.1016/j.jhydrol.2024.131568, 2024.

Bandai, T., Hamamoto, S., Rau, G.C., Komatsu, T., and Nishimura, T.: The effect of particle size on thermal and solute dispersion in saturated porous media. Int. J. Therm. Sci. 122, 74–84. https://doi.org/10.1016/j.ijthermalsci.2017.08.003, 2017.

Bear, J.: Dynamics of Fluids in Porous Media. Dover Publications, 1972.

Carslaw, H.S., Jaeger, J.C., Jaeger, J.C.J., 1959. Conduction of Heat in Solids, Oxford science publications. Clarendon Press.

Davis, J.M., Wilson, J.L., Phillips, F.M., and Gotkowitz, M.B.: Relationship between fluvial bounding surfaces and the permeability correlation structure. Water Resour. Res. 33, 1843–1854. https://doi.org/10.1029/97wr01003, 1997.

Davis, M.A., Walsh, S.D.C., and Saar, M.O.: Statistically reconstructing continuous isotropic and anisotropic two-phase media while preserving macroscopic material properties. Phys. Rev. E - Stat. Nonlinear, Soft Matter Phys. 83, 1–11. https://doi.org/10.1103/PhysRevE.83.026706, 2011.

de Marsily, G.: Quantitative Hydrogeology: Groundwater Hydrology for Engineers. San Diego, CA: Academic Press.

Dentz, M., Hidalgo, J.J., Lester, D., 2023. Mixing in Porous Media: Concepts and Approaches Across Scales, Transport in Porous Media. Springer Netherlands. https://doi.org/10.1007/s11242-022-01852-x, 1986.

Di Palma, P.R., Guyennon, N., Heße, F., and Romano, E.: Porous media flux sensitivity to pore-scale geostatistics: A bottom-up approach. Adv. Water Resour. 102, 99–110. https://doi.org/10.1016/j.advwatres.2017.02.002, 2017.

Fetter, C.W.: Applied Hydrogeology. 4th ed. Upper Saddle River, NJ: Prentice-Hall Inc, 2001.

Freeze, R.A., and Cherry, J.A.: Groundwater, 0-13-365312-9. Prentice-Hall, 1979.

Freyberg, L.: Dispersion of Nonreactive Tracers. Water Resour. Res. 22, 2031–2046, 1986.

Friedman, G.M., Sanders, J.E., and Sanders, J.E.: Principles of Sedimentology. Wiley., 1978.

Gelhar, L.W., Welty, C., and Rehfeldt, K.R.: A critical review of data on field-scale dispersion in aquifers. Water Resour. Res. 28(7), 1955–1974. https://doi.org/10.1029/92WR00607, 1992.

https://doi.org/10.5194/egusphere-2026-3736
Preprint. Discussion started: 7 August 2026

Gebhardt, H., Zech, A., Rau, G.C., and Bayer, P.: Effective thermal retardation in aquifers of heterogeneous hydraulic conductivity. Water Resources Research, 61(10), e2025WR040153. https://doi.org/10.1029/2025WR040153, 2025.

Ghanbarian, B., and Daigle, H.: Thermal conductivity in porous media: Percolation-based effective-medium approximation. Water Resources Research, 52(1), 295-314. https://doi:10.1002/2015WR017236, 2016.

Golovnina, S.: Modeling and Inversion in Weakly Anisotropic Media 1–134, 2004.

Gundersen, H. J. G., Boyce, R. W., Nyengaard, J. R., and Odgaard, A.: The Conneulor: unbiased estimation of connectivity using physical disectors under projection. Bone, 14(3), 217-222, 10.1016/8756-3282(93)90144-Y, 1993.

Hunt, B.: Dispersive sources in uniform ground-water flow. J. Hydraul. Div. 104, 75–85. https://doi.org/10.1061/jyceaj.0004925, 1978.

Ilgen, A.G., Borguet, E., Geiger, F.M., Gibbs, J.M., Grassian, V.H., Jun, Y.S., Kabengi, N., and Kubicki, J.D.: Bridging molecular-scale interfacial science with continuum-scale models. Nat. Commun. 15, 1–14. https://doi.org/10.1038/s41467-024-49598-y, 2024.

Irvine, D. J., Simmons, C. T., Werner, A. D., and Graf, T.: Heat and solute tracers: How do they compare in heterogeneous aquifers? Groundwater, 53(S1), 10-20. https://doi.org/10.1111/gwat.12146, 2015.

Irvine, D. J., Cartwright, I., Post, V. E., Simmons, C. T., and Banks, E. W.: Uncertainties in vertical groundwater fluxes from 1-D steady state heat transport analyses caused by heterogeneity, multidimensional flow, and climate change. Water Resour. Res., 52(2), 813-826. https://doi.org/10.1002/2015WR017702, 2016.

Irvine, D. J., Cranswick, R. H., Simmons, C. T., Shanafield, M. A., and Lautz, L. K.: The effect of streambed heterogeneity on groundwater-surface water exchange fluxes inferred from temperature time series. Water Resour. Res., 51(1), 198-212. https://doi.org/10.1002/2014WR015769, 2015.

Lee, H., Gossler, M., Zosseder, K., Blum, P., Bayer, P., and Rau, G.C.: Laboratory heat transport experiments reveal grain-size- and flow-velocity-dependent local thermal non-equilibrium effects. Hydrol. Earth Syst. Sci. 29, 1359–1378. https://doi.org/10.5194/hess-29-1359-2025, 2025.

Ma, R., Zheng, C., Zachara, J.M., Tonkin, M.: Utility of bromide and heat tracers for aquifer characterization affected by highly transient flow conditions. Water Resour. Res. 48, 8523. https://doi.org/10.1029/2011WR011281, 2012.

Matérn, B.: Spatial variation. Stochastic models and their application to some problems in forest surveys and other sampling investigations. Meddelanden från Statens Skogsforskningsinstitut, 49(5), 144 p., Stockholm, 1960.

Mehmani, Y., and Tchelepi, H.A.: Multiscale computation of pore-scale fluid dynamics: Single-phase flow. J. Comput. Phys. 375, 1469–1487. https://doi.org/10.1016/j.jcp.2018.08.045, 2018.

Mishra, P., Pandey, C.M., Singh, U., Gupta, A., Sahu, C., and Keshri, A.: Descriptive statistics and normality tests for statistical data. Ann. Card. Anaesth. 22, 67–72. https://doi.org/10.4103/aca.ACA_157_18, 2019.

Park, B.H., and Lee, K.K.: Evaluating anisotropy ratio of thermal dispersivity affecting geometry of plumes generated by aquifer thermal use. J. Hydrol. 602, 126740. https://doi.org/10.1016/j.jhydrol.2021.126740, 2021.

Park, B.H., Lee, B.H., and Lee, K.K.: Experimental investigation of the thermal dispersion coefficient under forced groundwater flow for designing an optimal groundwater heat pump (GWHP) system. J. Hydrol. 562, 385–396. https://doi.org/10.1016/j.jhydrol.2018.05.023, 2018.

Park, B.H.: Experimental and numerical investigation of thermal dispersion and its significance for designing groundwater heat pump (GWHP) systems. Seoul National University, 2019.

Pires, L. F., Auler, A. C., Roque, W. L., and Mooney, S. J.: X-ray microtomography analysis of soil pore structure dynamics under wetting and drying cycles. Geoderma, 362, 114103, https://doi.org/10.1016/j.geoderma.2019.114103, 2020.

Qu, M.L., Yang, J., Foroughi, S., Zhang, Y., Yu, Z.T., Blunt, M.J., and Lin, Q.: Pore-to-meter scale modeling of heat and mass transport applied to thermal energy storage: How local thermal and velocity fluctuations affect average thermal dispersivity. Energy 296, 131147. https://doi.org/10.1016/j.energy.2024.131147, 2024.

Raffensperger, J.P., and Vlassopoulos, D.: The potential for free and mixed convection in sedimentary basins. Hydrogeol. J. 7, 505–520. https://doi.org/10.1007/s100400050224, 1999.

Rau, G.C., Andersen, M.S., and Acworth, R.I.: Experimental investigation of the thermal dispersivity term and its significance in the heat transport equation for flow in sediments. Water Resour. Res. https://doi.org/10.1029/2011WR011038, 2012a.

Rau, G.C., Andersen, M.S., and Acworth, R.I.: Experimental investigation of the thermal time-series method for surface water-groundwater interactions. Water Resour. Res. 48(3), W03530. https://doi.org/10.1029/2011WR011560, 2012b.

Rau, G.C., Andersen, M.S., McCallum, A.M., Roshan, H., and Acworth, R.I.: Heat as a tracer to quantify water flow in near-surface sediments. Earth-Science Rev. https://doi.org/10.1016/j.earscirev.2013.10.015, 2014.

Roshan, H., Cuthbert, M.O., Andersen, M.S., and Acworth, R.I.: Local thermal non-equilibrium in sediments: Implications for temperature dynamics and the use of heat as a tracer. Adv. Water Resour. 73, 176–184. https://doi.org/10.1016/j.advwatres.2014.08.002, 2014.

Roque, W. L., Souza, A. C. A. D., and Barbieri, D. X.: The Euler-Poincaré characteristic applied to identify low bone density from vertebral tomographic images. Revista Brasileira de Reumatologia, 49, 140-145, https://doi.org/10.1590/S0482-50042009000200006, 2009.

Sarris, T.S., Close, M., and Abraham, P.: Using solute and heat tracers for aquifer characterization in a strongly heterogeneous alluvial aquifer. J. Hydrol. 558, 55–71. https://doi.org/10.1016/j.jhydrol.2018.01.032, 2018.

Schincariol, R.A., and Schwartz, F.W.: An experimental investigation of variable density flow and mixing in homogeneous and heterogeneous media. Water Resour. Res. 26, 2317–2329. https://doi.org/10.1029/WR026i010p02317, 1990.

Schwanghart, W., variogramfit. MATLAB Central File Exchange. Available at: https://www.mathworks.com/matlabcentral/fileexchange/25948-variogramfit (accessed 21 Jeune 2025), 2025.

Shi, W., Wang, Q., Klepikova, M., Irvine, D. J., Jin, A., and Wang, Y.: Effects of local thermal nonequilibrium and sediment heterogeneity on heat tracer-based downwelling flux quantification in streambeds. Water Resour. Res. 61(12), WR041536. https://doi.org/10.1029/2025WR041536, 2025.

https://doi.org/10.5194/egusphere-2026-3736
Preprint. Discussion started: 7 August 2026

Sole-Mari, G., Riva, M., Fernàndez-Garcia, D., Sanchez-Vila, X., and Guadagnini, A.: Solute transport in bounded porous media characterized by generalized sub-Gaussian log-conductivity distributions. Adv. Water Resour. 147, 103812. https://doi.org/10.1016/j.advwatres.2020.103812, 2021.

Stauffer, F., Bayer, P., Blum, P., Kinzelbach, W., and Giraldo, N.M.: Thermal Use of Shallow Groundwater, Environmental engineering. Taylor & Francis Group, 2017.

Sudicky, E. A.: A natural gradient experiment on solute transport in a sand aquifer: Spatial variability of hydraulic conductivity and its role in the dispersion process. Water Resour. Res., *22*(13), 2069-2082, https://doi.org/10.1029/WR022i013p02069, 1986.

Vandenbohede, A., Louwyck, A., and Lebbe, L.: Conservative solute versus heat transport in porous media during push-pull tests. Transp. Porous Media 76, 265–287. https://doi.org/10.1007/s11242-008-9246-4, 2009.

Vitagliano, V., and Lyons, P.A.: Diffusion coefficients for aqueous solutions of sodium chloride and barium chloride. J. Am. Chem. Soc. 78, 1549–1552. https://doi.org/10.1021/ja01589a011, 1956.

Vogel, H. J., and Roth, K.: Quantitative morphology and network representation of soil pore structure. Advances in water resources, 24(3-4), 233-242, 2001.

Yang, C., and Nakayama, A.: A synthesis of tortuosity and dispersion in effective thermal conductivity of porous media. Int. J. Heat Mass Transf. 53, 3222–3230. https://doi.org/10.1016/j.ijheatmasstransfer.2010.03.004, 2010.

Yin, M., Ma, R., Zhang, Y., Lin, J., Guo, Z., and Zheng, C.: Competitive control of multiscale aquifer heterogeneity on solute transport in an alluvial aquifer. J. Hydrol. 616, 128819. https://doi.org/10.1016/j.jhydrol.2022.128819, 2023.

Zech, A., Dietrich, P., Attinger, S., and Teutsch, G.: A field evidence model: How to predict transport in heterogeneous aquifers at low investigation level. Hydrol. Earth Syst. Sci. 25, 1–15. https://doi.org/10.5194/hess-25-1-2021, 2021.

Zhang, X., Ma, F., Yin, S., Wallace, C.D., Soltanian, M.R., Dai, Z., Ritzi, R.W., Ma, Z., Zhan, C., and Lü, X.: Application of upscaling methods for fluid flow and mass transport in multi-scale heterogeneous media: A critical review. Appl. Energy 303, 117603. https://doi.org/10.1016/j.apenergy.2021.117603, 2021.